

1  
2  
3  
4  
5  
6  
7  
8  
9  
10  
11  
12  
13  
14  
15  
16  
17  
18  
19  
20  
21

**Distinct mesoderm migration phenotypes in extra-embryonic and embryonic regions of the early mouse embryo**

Bechara Saykali<sup>1</sup>, Navrita Mathiah<sup>1\*</sup>, Wallis Nahaboo<sup>1\*</sup>, Marie-Lucie Racu<sup>1</sup>,  
Matthieu Defrance<sup>2</sup>, and Isabelle Migeotte<sup>1, 3, 4</sup>

<sup>1</sup>Université Libre de Bruxelles, IRIBHM, Brussels B-1070

<sup>2</sup>Université Libre de Bruxelles, Computer Science Department, Brussels B-1050

<sup>3</sup>WELBIO

<sup>4</sup>Correspondence should be addressed to I.M. (e-mail: [imigeott@ulb.ac.be](mailto:imigeott@ulb.ac.be)).

\*These authors contributed equally to this work.

22 **ABSTRACT**

23 In the gastrulating mouse embryo, epiblast cells delaminate at the primitive streak to  
24 form mesoderm and definitive endoderm, through an epithelial-mesenchymal transition.

25  
26 Mosaic expression of a membrane reporter in nascent mesoderm enabled recording cell  
27 shape and trajectory through live imaging. Upon leaving the streak, cells changed shape  
28 and extended protrusions of distinct size and abundance depending on the neighboring  
29 germ layer, as well as the region of the embryo. Embryonic trajectories were meandering  
30 but directional, while extra-embryonic mesoderm cells showed little net displacement.

31  
32 Embryonic and extra-embryonic mesoderm transcriptomes highlighted distinct guidance,  
33 cytoskeleton, adhesion, and extracellular matrix signatures. Specifically, intermediate  
34 filaments were highly expressed in extra-embryonic mesoderm, while live imaging for F-  
35 actin showed abundance of actin filaments in embryonic mesoderm only. Accordingly,  
36 *RhoA* or *Rac1* conditional deletion in mesoderm inhibited embryonic, but not extra-  
37 embryonic mesoderm migration.

38  
39 Overall, this indicates separate cytoskeleton regulation coordinating the morphology and  
40 migration of mesoderm subpopulations.

41

## 42 **INTRODUCTION**

43 In mice, a first separation of embryonic and extra-embryonic lineages begins in the  
44 blastocyst at embryonic day (E) 3.5 when the trophectoderm is set aside from the inner  
45 cell mass. A second step is the segregation of the inner cell mass into the epiblast, the  
46 precursor of most fetal cell lineages, and the extra-embryonic primitive endoderm  
47 (Chazaud & Yamanaka, 2016). At E6, the embryo is cup-shaped and its anterior-  
48 posterior axis is defined. It comprises three cell types, arranged in two layers: the inner  
49 layer is formed by epiblast, distally, and extra-embryonic ectoderm, proximally; the outer  
50 layer, visceral endoderm, covers the entire embryo surface. The primitive streak, site of  
51 gastrulation, is formed at E6.25 in the posterior epiblast, at the junction between  
52 embryonic and extra-embryonic regions, and subsequently elongates to the distal tip of  
53 the embryo. The primitive streak is the region of the embryo where epiblast cells  
54 delaminate through epithelial-mesenchymal transition to generate a new population of  
55 mesenchymal cells that form the mesoderm and definitive endoderm layers.

56  
57 All mesoderm, including the extra-embryonic mesoderm, is of embryonic epiblast origin.  
58 At the onset of gastrulation, emerging mesoderm migrates either anteriorly as so-called  
59 embryonic mesodermal wings, or proximally as extra-embryonic mesoderm (Arnold &  
60 Robertson, 2009; Sutherland, 2015). Cell lineages studies showed that there is little  
61 correlation between the position of mesoderm progenitors in the epiblast and the final  
62 localization of mesoderm descendants (Lawson, Meneses, & Pedersen, 1991). Rather,  
63 the distribution of mesoderm subpopulations depends on the temporal order and  
64 anterior-posterior location of cell recruitment through the primitive streak (Kinder et al.,  
65 1999). Posterior primitive streak cells are the major source of extra-embryonic  
66 mesoderm, while cells from middle and anterior primitive streak are mostly destined to  
67 the embryo proper. However, there is overlap of fates between cells delaminating at  
68 different sites and timings (Kinder et al., 1999, 2001). Extra-embryonic mesoderm  
69 contributes to the amnion, allantois, chorion, and visceral yolk sac. It has important  
70 functions in maternal-fetal protection and communication, as well as in primitive  
71 erythropoiesis (Watson, 2005). Embryonic mesoderm separates into lateral plate,  
72 intermediate, paraxial and axial mesoderm, and ultimately gives rise to cranial and

73 cardiac mesenchyme, blood vessels and hematopoietic progenitors, urogenital system,  
74 muscles and bones, among others. Endoderm precursors co-migrate with mesoderm  
75 progenitors in the wings and undergo a mesenchymal-epithelial transition to intercalate  
76 into the visceral endoderm (Viotti, Foley, & Hadjantonakis, 2014).

77  
78 Mesoderm migration mechanisms have mostly been studied in fly, fish, frog and chicken  
79 embryos. Interestingly, during fly gastrulation, mesodermal cells migrate as a collective  
80 (Bae, Trisnadi, Kadam, & Stathopoulos, 2012). In the fish prechordal plate, all cells have  
81 similar migration properties but they require contact between each other for directional  
82 migration (Dumortier, Martin, Meyer, Rosa, & David, 2012). Live imaging experiments in  
83 chick suggest a collective mode of migration, even though cells frequently make and  
84 break contacts with their neighbors (Chuai, Hughes, & J. Weijer, 2012).

85  
86 Relatively little is known about mesoderm migration in mice because most mutant  
87 phenotypes with mesodermal defects result from anomalies in primitive streak formation,  
88 mesoderm specification, or epithelial-mesenchymal transition (Arnold & Robertson,  
89 2009), precluding further insight into cell migration mechanisms. We previously identified  
90 a role for the Rho GTPase Rac1, a mediator of cytoskeletal reorganization, in mesoderm  
91 migration and adhesion (Migeotte, Grego-Bessa, & Anderson, 2011).

92  
93 Recent advances in mouse embryo culture and live imaging have overcome the  
94 challenge of maintaining adequate embryo growth and morphology while performing  
95 high-resolution imaging. It facilitated the uncovering of the precise spatial and temporal  
96 regulation of cellular processes and disclosed that inaccurate conclusions had  
97 sometimes been drawn from static analyses (Viotti et al., 2014). Live imaging of mouse  
98 embryos bearing a reporter for nuclei has pointed towards individual rather than  
99 collective migration in the mesodermal wings (Ichikawa et al., 2013). Very recently, a  
100 spectacular adaptive light sheet imaging approach allowed reconstructing fate maps at  
101 the single cell level from gastrulation to early organogenesis (McDole et al., 2018).  
102 However, little is known about how mesoderm populations regulate their shape and  
103 migration mechanisms as they travel across distinct embryo regions to fulfill their

104 respective fates.

105  
106 Here, high-resolution live imaging of nascent mesoderm expressing membrane-bound  
107 GFP was used to define the dynamics of mesoderm cell morphology and its trajectories.  
108 Mesoderm cells exhibited a variety of cell shape changes determined by their spatial  
109 localization in the embryo, and the germ layer they were in contact with. The embryonic  
110 mesoderm migration path was meandering but directional, and depended on the Rho  
111 GTPases RhoA and Rac1. Extra-embryonic mesoderm movement was, strikingly,  
112 GTPases independent. Transcriptomes of different mesoderm populations uncovered  
113 specific sets of guidance, adhesion, cytoskeleton and matrix components, which may  
114 underlie the remarkable differences in cell behavior between mesoderm subtypes.

115

## 116 **RESULTS**

### 117 *Mesoderm migration mode and cell shape differ in embryonic versus extra-embryonic* 118 *regions*

119 The T box transcription factor *Brachyury* is expressed in posterior epiblast cells that form  
120 the primitive streak, maintained in cells that delaminate through the streak, then down-  
121 regulated once cells progress anteriorly in the mesodermal wings (Wilkinson, Bhatt, &  
122 Herrmann, 1990). In order to visualize nascent mesoderm, *T(s)::Cre* (hereafter referred  
123 to as *T-Cre*) transgenic animals, in which Cre expression is driven by the regulatory  
124 elements of the *Brachyury* gene (Feller, Schneider, Schuster-Gossler, & Gossler, 2008;  
125 Stott, Kispert, & Herrmann, 1993), were crossed to a membrane reporter line:  
126 *Rosa26::membrane dtTomato/membrane GFP* (Muzumdar, Tasic, Miyamichi, Li, & Luo,  
127 2007) (referred to as mTmG) (Fig. 1). In *T-Cre*; mTmG embryos, primitive streak and  
128 mesoderm derived cells have green membranes (mG), whereas all other cells have red  
129 membranes (mT). Embryos dissected at E6.75 or E7.25 were staged according to (K M  
130 Downs & Davies, 1993) (Sup. Fig. 1a) and examined in different orientations by confocal  
131 or two-photon excitation live imaging for 8 to 12 hours (Fig. 1, Sup. Fig. 1b and c, Videos  
132 1 and 2). Conversion of mT to mG was first observed at Early/Mid Streak (E/MS) stage,  
133 and was initially mosaic, which facilitated the tracking of individual migrating cells with

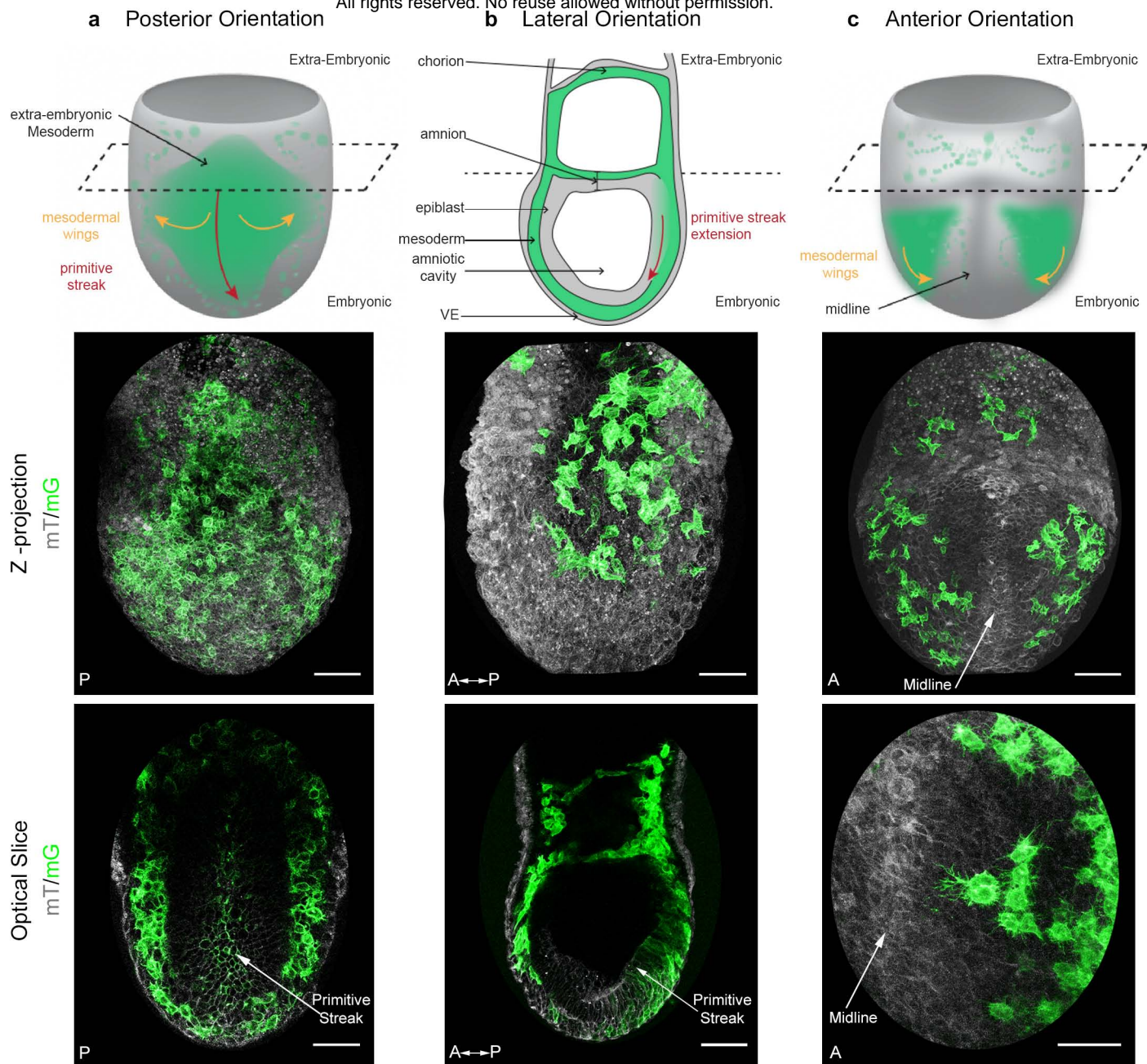


**Figure 1: Mosaic membrane GFP labeling of nascent mesoderm allows following individual cell migration through embryo live imaging.** (a) Posterior view. Top: 3D scheme with mesoderm layer in green and the rest of the embryo in grey. The dashed line separates embryonic and extra-embryonic regions. Middle: Z-projection of two-photon stack. Bottom: optical slice highlighting the primitive streak. (b) Lateral view, anterior to the left. Top: 2D scheme. Middle: Z-projection of two-photon stack showing cells progression from posterior to anterior. Bottom: sagittal optical slice. (c) Anterior view. Top: 3D scheme. Middle: Z-projection of two-photon stack with most anterior cells reaching the midline. Bottom: optical slice zoomed on filopodia extending towards the midline. All embryos were dissected at E7.25 and are at Late Streak/Zero Bud stage. VE: Visceral Endoderm; mG: membrane GFP, in green; mT: membrane dtTomato, in grey. (Scale bars: 50  $\mu$ m).

134 high cell shape resolution. From Mid/Late Streak (M/LS) onwards, most primitive streak  
135 cells underwent red to green conversion (Sup. Fig. 1d, e).

136  
137 The shape of mesoderm cells and their tracks were recorded through imaging of  
138 embryos from different perspectives between ES and Early Bud (EB) stages of  
139 development, in order to obtain images of optimal quality for each embryo region (Fig. 1  
140 and Videos 1 and 2). Posterior views (Fig. 1a) showed proximal to distal primitive streak  
141 extension and rounding of cells exiting the streak. Lateral views (Fig. 1b) allowed  
142 comparing cells as they migrated laterally in mesodermal wings, or proximally in extra-  
143 embryonic region. Anterior views (Fig. 1c) showed cell movement towards the midline.  
144 The imaging time frame did not allow following individual cells from their exit at the  
145 primitive streak to their final destination. However, the trajectories we acquired fitted with  
146 the fate maps built using cellular labeling or transplantation (Kinder et al., 1999, 2001),  
147 or adaptive light sheet microscopy (McDole et al., 2018) (Videos 3 and 4). The first  
148 converted (GFP positive) cells in ES embryos dissected around E6.75 usually left the  
149 posterior site of the primitive streak to migrate towards the extra-embryonic  
150 compartment. Embryonic migration started almost simultaneously, and migration  
151 towards both regions proceeded continuously.

152  
153 Strikingly, migration behavior (Fig. 2a, Videos 3 and 4) and cell shape (Fig. 2b) were  
154 different depending on the region cells migrated into. In the embryonic region,  
155 mesoderm cells had a global posterior to anterior path, even though they zigzagged in  
156 all directions (proximal-distal, left-right, and even anterior-posterior). Cells did not  
157 migrate continuously, but showed alternations of tumbling behavior with straighter  
158 displacement. Embryonic mesoderm cells from ES/MS embryos tracked for 2.5 h moved  
159 at a mean speed of 0.65  $\mu\text{m}/\text{min}$  to cover approximately 90  $\mu\text{m}$  and travel a net distance  
160 of 40  $\mu\text{m}$  (Fig. 2a', Table 1). Straightness (the ratio of net over travel displacement, so  
161 that a value of 1 represents a linear path) was approximately 0.5 (Fig. 2a', Table 1).  
162 Cells in the extra-embryonic region moved slightly slower (0.45  $\mu\text{m}/\text{min}$ ) to do  
163 approximately 70  $\mu\text{m}$ , but their net displacement (20  $\mu\text{m}$ ) and straightness (0.3) were

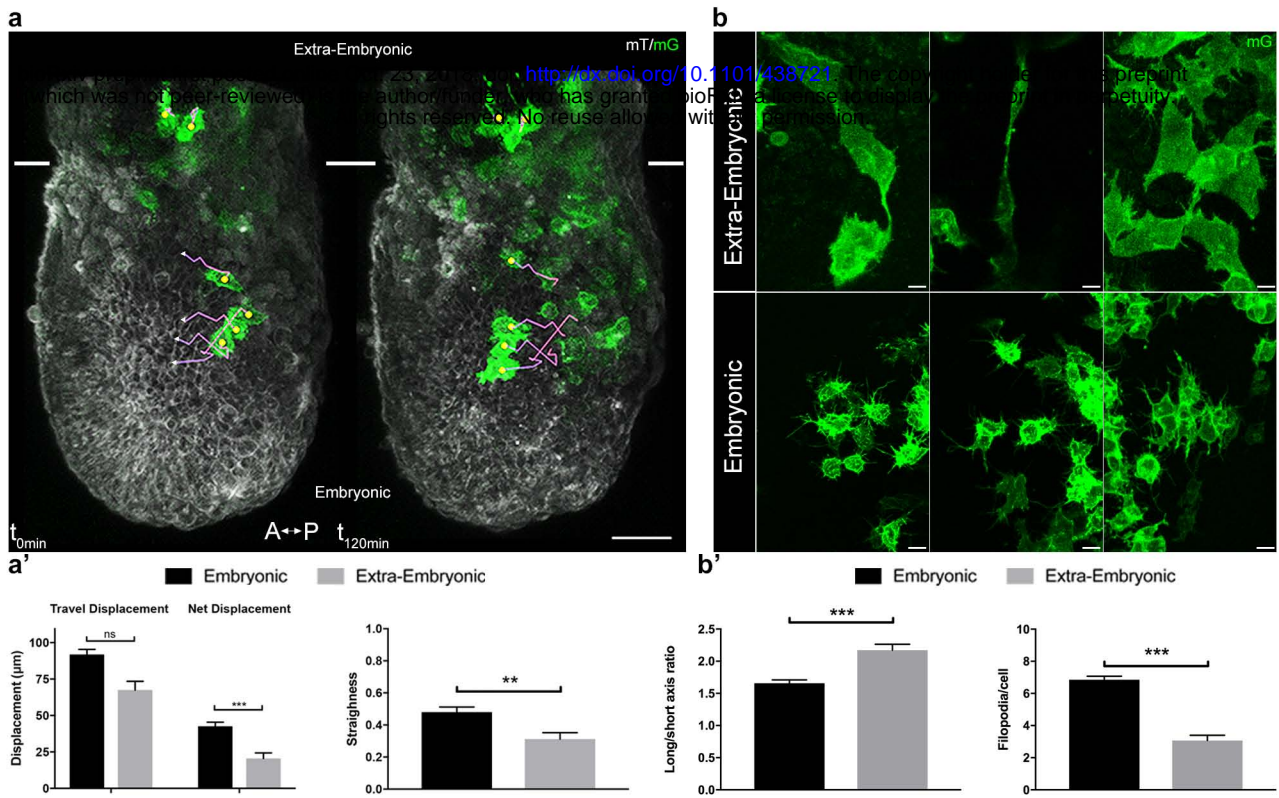


**Figure 2: Embryonic and extra-embryonic mesoderm populations have different morphology and migration pattern.** (a) Z-projections of confocal stacks from a *T-cre*; mTmG embryo dissected at E6.75 (Early Streak), with cell migration tracking for 120 min. Anterior to the left. White lines mark the embryonic/extra-embryonic boundary. (Scale bar: 50  $\mu\text{m}$ ). (a') Quantification (mean  $\pm$  SEM) of travel and net displacement (Left) and path straightness (Right, on a scale of 0 to 1) of embryonic (black,  $n=34$  from 4 Early/Mid Streak embryos) and extra-embryonic (grey,  $n=17$  cells) mesoderm cells. Data can be found in Table 1 and Source Data 1. (b) Embryonic and extra-embryonic mesoderm cell shapes (images extracted from 4 Late Streak embryos) (Z-projections of two-photon stacks, scale bar: 10  $\mu\text{m}$ ). (b') Left: Long/short axis ratio of 2D inner ellipse as quantification of cell stretch (mean  $\pm$  SEM,  $n=85$  embryonic cells in black,  $n=83$  extra-embryonic cells in grey, out of 8 Mid Streak to Zero Bud stages embryos). Right: Quantification (mean  $\pm$  SEM) of number of filopodia per cell in embryonic (black,  $n=167$  cells out of 5 Mid Streak to Early Bud stages embryos) and extra-embryonic (grey,  $n=28$  cells) mesoderm cells. Data can be found in Table 2, Source Data 2 and 3. *P* values were calculated using the Mann–Whitney–Wilcoxon. mG: membrane GFP, in green; mT: membrane dtTomato, in grey.

	Net displacement ( $\mu\text{m}$ )		Travel displacement ( $\mu\text{m}$ )		Straightness		Mean speed ( $\mu\text{m}/\text{min}$ )		N
	Mean	SEM	Mean	SEM	Mean	SEM	Mean	SEM	
Extra-embryonic	20,58	3,74	67,50	6,01	0,31	0,04	0,44	0,03	17
Embryonic	12,54	2,79	91,89	9,51	0,48	0,03	0,67	0,03	34
P-value	7,93E-05		5,99E-01		2,48E-03		2,00E-06		

**Table 1: Tracking details for embryonic and extra-embryonic mesoderm.** Cells were tracked for approximately 150 min. *P* values were calculated using the Mann–Whitney–Wilcoxon. Data can be found in Source Data 1.

	Volume ( $\mu\text{m}^3$ )		Surface ( $\mu\text{m}^2$ )		Long/short axis		N	Filopodia/cell		Filopodia length ( $\mu\text{m}$ )		N
	Mean	SEM	Mean	SEM	Mean	SEM		Mean	SEM	Mean	SEM	
Extra-embryonic	4253,03	234,80	2438,82	105,59	2,17	0,09	83	3,07	0,32	6,20	0,37	28
Embryonic	2002,08	81,36	1308,63	39,14	1,65	0,05	85	6,85	0,21	8,00	0,14	167
P-value	3,82E-17		5,41E-19		3,04E-05			3,28E-11		5,24E-04		

**Table 2: Cell shape, size, and filopodia comparison between embryonic and extra-embryonic mesoderm.** *P* values were calculated using the Mann–Whitney–Wilcoxon for surface, long/short axis and filopodia/cell, and the *t* test for volume, and filopodia length. Data can be found in Source Data 2 and 3.

164 significantly smaller, reflecting trajectories with no obvious directionality (Fig. 2a', Table  
165 1, and Video 5).

166

167 Extra-embryonic cells were stretched, sometimes spanning the entire width of the  
168 embryo, and twice larger (Fig. 2b, b', Table 2). They had few large protrusions, and  
169 filopodia were scarce and short (Fig. 2b, b', Table 2).

170

171 *Mesoderm cells have distinct morphology depending on their interaction with different*  
172 *germ layers*

173 Cells passing through the primitive streak were, as reported (Ramkumar et al., 2016; M.  
174 Williams, Burdsal, Periasamy, Lewandoski, & Sutherland, 2012), bottle shaped with a  
175 basal round cell body and an apical thin projection (Fig. 3a). Mesoderm cells in contact  
176 with the epiblast and visceral endoderm sent thin protrusions towards their respective  
177 basal membranes (Fig. 3b, b', and Video 6). Interestingly, the density of thin protrusions  
178 was much higher in cells in contact with the visceral endoderm; this phenotype was  
179 observed as early as ES, while intercalation of prospective definitive endoderm cells in  
180 the visceral endoderm layer occurred only from LS stage onwards (Viotti et al., 2014).

181 Cells in tight clusters surrounded by other mesoderm cells in the wings had a smoother  
182 contour. A caveat was that protrusions couldn't be visualized between two cells of  
183 similar membrane color. Reconstruction of cells in the anterior part of the wings, where  
184 recombination was incomplete, showed thin protrusions between mesoderm cells. Cells  
185 also extended long broad projections, which spanned several cell diameters and were  
186 sent in multiple directions before translation of the cell body, in what seemed a trial and  
187 error process (Fig. 3c and Videos 1, 2 and 7). The presence of potential leader cells  
188 could not be assessed, as the first cells converted to green are not the most anterior  
189 ones (Sup. Fig. 1d). Nonetheless, cells with scanning behavior were observed at all  
190 times, which suggests that all cells are capable to explore their surroundings.

191

192 *Cell-cell communication within the mesoderm layer*

193 As expected from fate mapping experiments, daughter cells resulting from mitosis within  
194 the mesoderm layer followed close and parallel trajectories (Fig. 3d and Source Data 5).

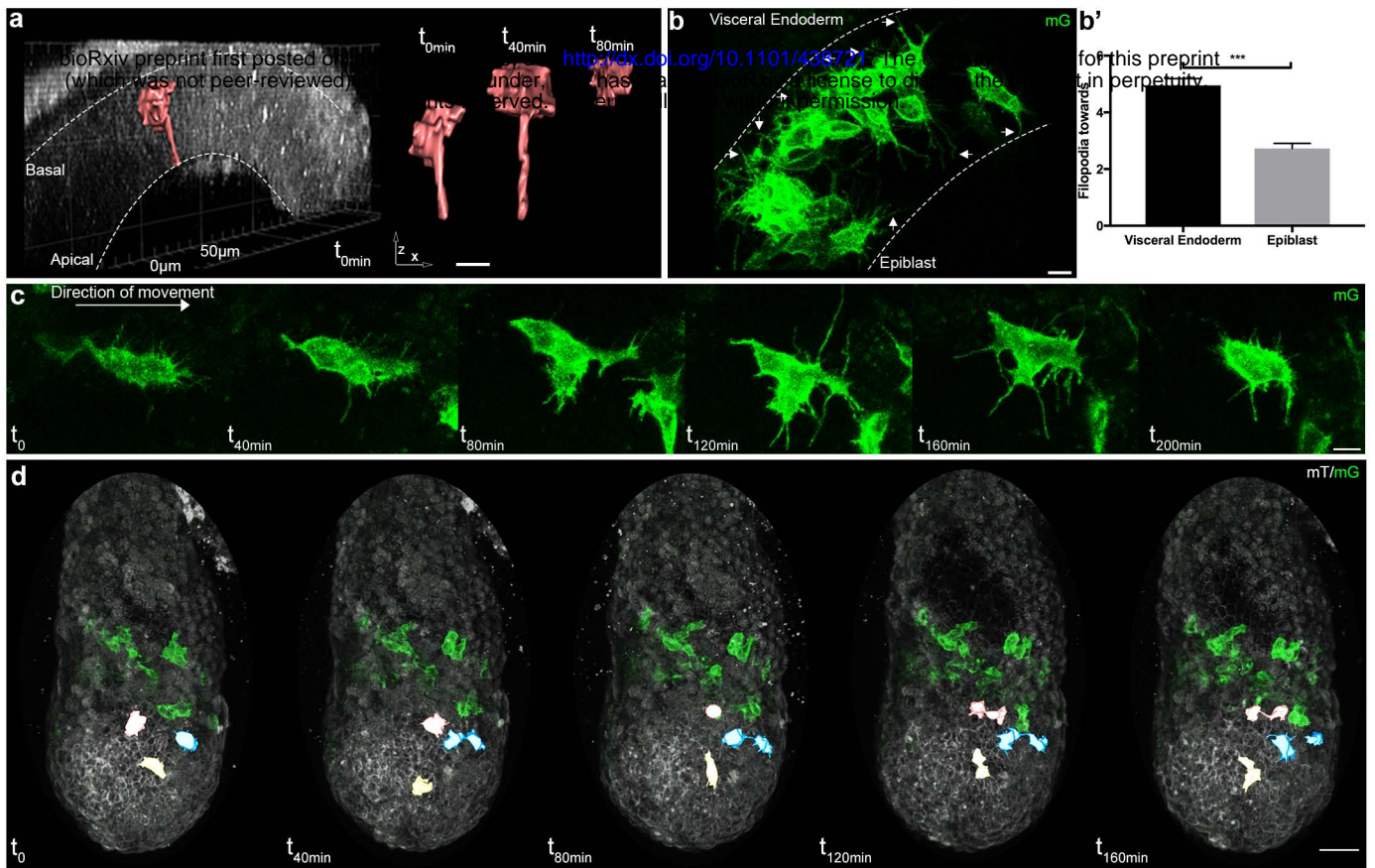


**Figure 3: Cell shape changes of migrating mesoderm.** (a) Cell shape progression of nascent mesoderm delaminating at the primitive streak of a Mid Streak embryo (Z-projection of two-photon stack, scale bar: 10  $\mu\text{m}$ ). (b) Mesoderm cells extend filopodia (arrows) towards epiblast and visceral endoderm. Embryo is at Late Streak stage. (Z-projection of two-photon stack, scale bar: 10  $\mu\text{m}$ ). (b') Quantification of filopodia (filopodia per cell, mean  $\pm$  SEM,  $n=40$  cells out of 4 Late Streak embryos for each,  $p<0.0001$ ).  $P$  value was calculated using the  $t$  test. Data can be found in Source Data 4. (c) Montage of a mesoderm cell (from a Mid Streak stage embryo) displaying seeking behavior (Z-projection of two-photon stack, scale bar: 10  $\mu\text{m}$ ). (d) Mesoderm cells are highlighted, through manual segmentation, in red, blue and yellow to track cell behavior after division (Z-projection of confocal stacks from a Mid Streak stage embryo, anterior view, scale bar: 50  $\mu\text{m}$ ). mG: membrane GFP, in green; mT: membrane dtTomato, in grey.

195 They travelled a similar net distance over 204 min (net displacement ratio:  $0.91 \pm 0.01$ ,  
196  $n=12$  pairs from four embryos at E/MS stage), in the same direction (angle:  $7 \pm 1.13^\circ$ ),  
197 with one daughter cell displaying a higher straightness (travel displacement ratio:  $0.61 \pm$   
198  $0.07$ ). They remained close to one another (mean distance between daughter cells:  $15.6$   
199  $\pm 2.35 \mu\text{m}$ ), but not directly apposed. Interestingly, they stayed linked by thin projections  
200 for hours, even when separated by other cells (Fig. 3d).

201  
202 Mesoderm cell migration is often compared to neural crest migration, as both cell types  
203 arise through epithelial-mesenchymal transition (Roycroft & Mayor, 2016). An important  
204 feature of neural crest migration is contact inhibition of locomotion, where cells that  
205 collide tend to move in opposite directions. In contrast, most mesoderm cells stayed in  
206 contact upon collision (Source Data 6): 16 out of 24 cell pairs from 5 ES to Zero Bud  
207 (0B) embryos remained attached for 2.5 hour (one briefly lost contact before re-joining),  
208 3/24 stayed joined for around 1 hour, and 5/24 pairs separated instantly. We segmented  
209 8 pairs for 166 min, and observed a mean distance at the end of tracking of  $52.5 \pm 32.5$   
210  $\mu\text{m}$ ; they followed parallel trajectories (angle:  $8.25 \pm 1.7^\circ$ ,  $n=8$  pairs), for a similar net  
211 distance (net displacement ratio:  $0.85 \pm 0.07$ ; travel displacement ratio:  $0.64 \pm 0.11$ ).  
212 Thin projections could occasionally be observed between them after contact.

### 213 214 *Embryonic and extra-embryonic mesoderm molecular signatures*

215 Embryonic and extra-embryonic mesoderm cells were isolated through fluorescence  
216 (GFP)-assisted cell sorting from E7.5 MS and LS *T-Cre*; mT/mG embryos in order to  
217 generate transcriptomes. Biological replicates (4 MS, 2 LS) from both stages resulted in  
218 grouping of samples according to the embryonic region (Fig. 4a, b). Non-supervised  
219 clustering based on embryonic and extra-embryonic gene signatures identified by single  
220 cell sequencing in (Scialdone et al., 2016) showed that samples segregated as expected  
221 (not shown). We performed pairwise comparison of embryonic and extra-embryonic  
222 samples obtained at both stages and selected the genes that were consistently  
223 differentially expressed with a fold change  $> 2$ . Gene ontology analysis showed  
224 significant enrichment in expected cellular (transcription and differentiation),  
225 developmental (angiogenesis, heart development, somitogenesis, and hematopoiesis),

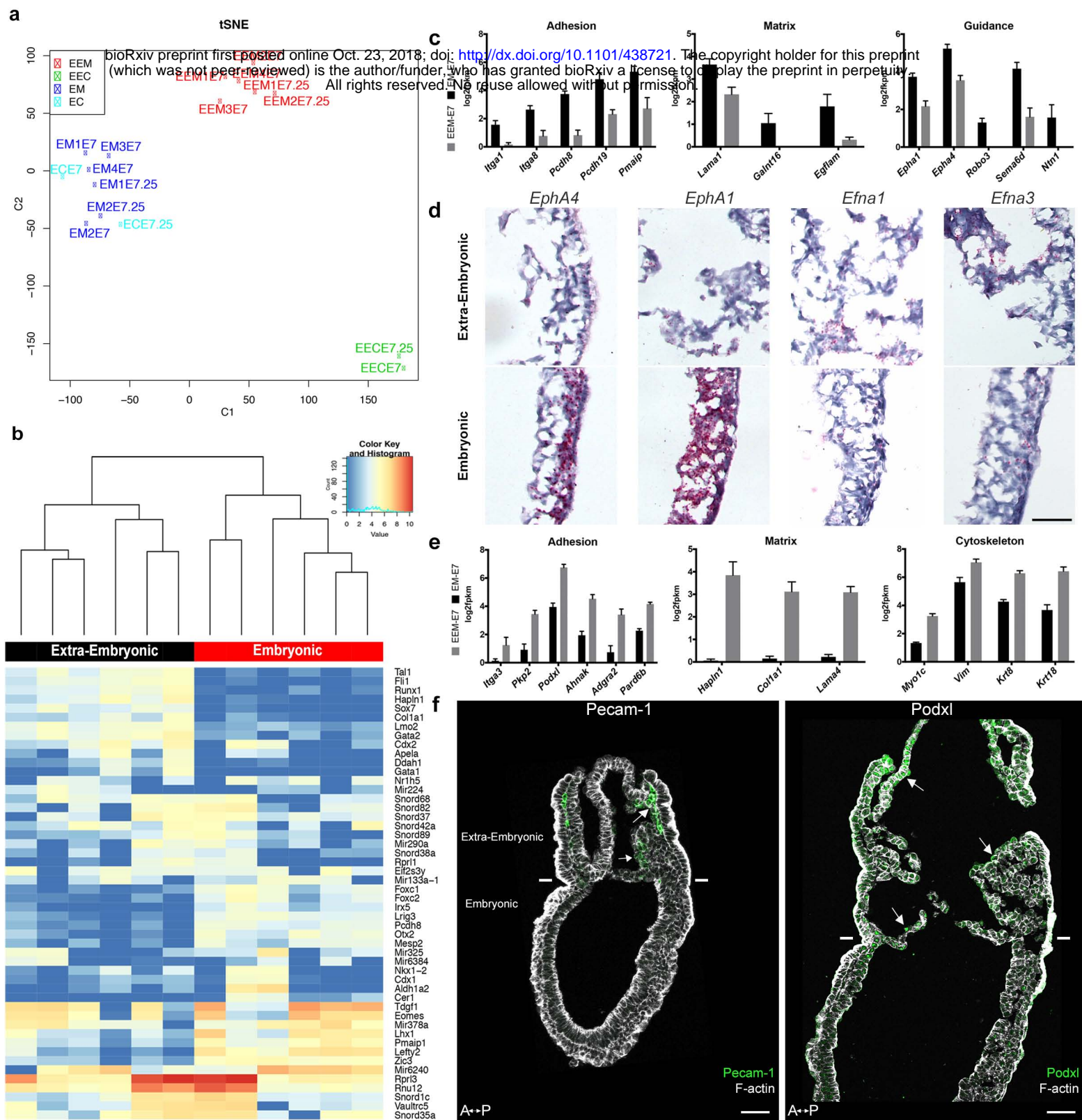


**Figure 4: Transcriptomes of mesoderm populations identify differences between embryonic and extra-embryonic mesoderm.** (a) t-Distributed Stochastic Neighbor Embedding (t-SNE) confirms grouping of similar biological samples at E7 (Mid Streak stage) and E7.25 (Late Streak stage). EM: Embryonic mesoderm; EEM: Extra-Embryonic mesoderm; EC: Embryonic control; EEC: Extra-Embryonic control. More sample information can be found in Source Data 7. (b) Heat map showing differentially expressed genes between embryonic and extra-embryonic mesoderm with the highest statistical significance. (c, e) Selection of genes with higher expression in embryonic (c) or extra-embryonic (e) mesoderm, represented as mean  $\pm$  SEM of log2 fpkm at E7 (n=4 biological replicates, p<0.01), with embryonic in black and extra-embryonic in grey. All represented genes are also significantly differentially regulated at E7.25. Data can be found in Source Data 8 and 9. (d) *In situ* hybridization of sagittal sections (anterior to the left) from Zero to Early Bud stages embryos highlighting transcripts for *Epha4*, *Epha1*, *Efna1* and *Efna3*, represented by red dots, in the posterior region. Entire embryo sections are shown in Sup. Fig. 2. (Scale bar: 100  $\mu$ m) (f) Sagittal sections (anterior to the left) from Early Bud stage embryos stained for Platelet endothelial cell adhesion molecule 1 (left panel, Pecam-1 in green, Z-projection of confocal stack), Podocalyxin (right panel, Podxl in green, optical slice), and F-actin (Phalloidin, grey). See same section stained for mGFP in Sup. Fig. 2. White lines mark the embryonic/extra-embryonic boundary. (Scale bars: 50  $\mu$ m).

226 and signaling (Wnt, BMP and Notch) biological processes. Interestingly, differences  
227 were also seen in gene clusters involved in migration, adhesion, matrix organization,  
228 and small GTPases mediated signal transduction (Sup. Fig. 2a).

229  
230 Genes with known expression pattern in gastrulating embryos found enriched in  
231 embryonic mesoderm included well-described transcription factors, as well as FGF, Wnt,  
232 Notch, TGF $\beta$  and Retinoic Acid effectors (Sup. Fig. 2b). Genes expected to be more  
233 expressed in extra-embryonic mesoderm included the transcription factors *Ets1* and  
234 *Tbx20*, and several members of the TGF $\beta$  pathway (Inman & Downs, 2007; Pereira et  
235 al., 2011) (Sup. Fig. 2c). Primitive hematopoiesis, the initial wave of blood cell  
236 production which gives rise to primitive erythrocytes, macrophages, and  
237 megakaryocytes, takes place around E7.25 in hemogenic angioblasts of the blood  
238 islands (Lacaud & Kouskoff, 2017). Expression of genes involved in hemangioblast  
239 development, endothelium differentiation, and hematopoiesis increased from MS to LS  
240 (Fig. 4f and Sup. Fig. 2c). In addition, we confirmed two extra-embryonic genes  
241 identified through subtractive hybridization at E7.5 (Kingsley et al., 2001): *Ahnak* (Sup.  
242 Fig. 2c, see also (Karen M. Downs, McHugh, Copp, & Shtivelman, 2002)) and the  
243 imprinted gene *H19* (Sup. Fig. 2c).

244  
245 Of particular interest among the genes with higher expression in embryonic mesoderm  
246 for which no expression data was available at the stage of development were genes  
247 related to matrix (*Lama1*, *Galnt16*, *Egflam*), adhesion (*Itga1*, *Itga8*, *Pcdh8*, *Pcdh19*,  
248 *Pmaip1*), and guidance (*Epha1* and 4, *Robo3*, *Sema6d*, *Ntn1*) (Fig. 4c). *Epha4*  
249 expression in the mouse embryo has been described in the trunk mesoderm and  
250 developing hindbrain at Neural Plate (NP) stage (M A Nieto, Gilardi-Hebenstreit,  
251 Charnay, & Wilkinson, 1992). In LS embryos, *Epha4* expression was higher in the  
252 primitive streak and embryonic mesoderm (Fig. 4d and Sup. Fig. 2e). Dynamic *Epha1*,  
253 *Efna1* and *Efna3* expression patterns have been shown during gastrulation (Duffy,  
254 Steiner, Tam, & Boyd, 2006). In LS/0B embryos, *Epha1* mRNA was present in the  
255 primitive streak, mostly in its distal part. Its ligand *Efna1* was in the primitive streak with  
256 an inverse gradient, and was mainly expressed in the extra-embryonic region, notably in

257 amnion and in chorion. *Efna3* was very abundant in the chorion (Fig. 4d and Sup. Fig.  
258 2e).

259  
260 In parallel, in extra-embryonic mesoderm, we found higher expression of distinct sets of  
261 genes with putative roles in guidance (*Unc5c*, *Dlk1*, *Scube2*, *Fzd4*), matrix composition  
262 (*Hapln1*, *Col1a1*, *Lama4*), adhesion (*Itga3*, *Pkp2*, *Podxl*, *Ahnak*, *Adgra2*, *Pard6b*), Rho  
263 GTPase regulation (*Rasip1*, *Stard8*, *RhoJ*), and cytoskeleton (*Myo1c*, *Vim*, *Krt8* and  
264 *Krt18*) (Fig. 4e and not shown). Interestingly, Podocalyxin (*Podxl*) was abundant in  
265 extra-embryonic mesoderm (Fig. 4f and Sup. Fig. 2d), which fits with data from embryo  
266 and embryoid body single cell sequencing showing that *Podxl* is a marker for early  
267 extra-embryonic mesoderm and primitive erythroid progenitors of the yolk sac (Zhang et  
268 al., 2014).

269  
270 *Embryonic and extra-embryonic mesoderm cells have distinct cytoskeletal composition*  
271 In view of the differences in cell shape and migration, we focused on the cytoskeleton, in  
272 particular actin, and intermediate filaments proteins (Vimentin and Keratins). Vimentin  
273 was found in all mesoderm cells as expected, but more abundant in extra-embryonic  
274 mesoderm (Fig. 5a). Remarkably, within the mesoderm layer, Keratin 8 was selectively  
275 expressed in extra-embryonic mesoderm cells (amniochorionic fold, amnion, chorion,  
276 and developing allantois) (Fig. 5b-d). In contrast, the filamentous actin (F-actin) network,  
277 visualized by Phalloidin staining, seemed denser in embryonic mesoderm (Fig. 5a). To  
278 visualize F-actin only in mesoderm, we took advantage of a conditionally inducible  
279 mouse model expressing Lifeact-GFP, a peptide that binds specifically to F-actin with  
280 low affinity, and thus reports actin dynamics without disrupting them (Schachtner et al.,  
281 2012). Live imaging of *T-Cre*; LifeAct-GFP embryos at MS and LS stage confirmed that  
282 while LifeAct-GFP positive filaments could be visualized clearly in embryonic mesoderm  
283 cells, GFP was weaker and diffuse in extra-embryonic mesoderm (Fig. 5e and Video 8).

284  
285 *Extra-embryonic mesoderm migration is Rho GTPases independent*  
286 Rho GTPases are molecular switches that relay signals from cell surface receptors to  
287 intracellular effectors, leading to a change in cell behavior (Hodge & Ridley, 2016). They

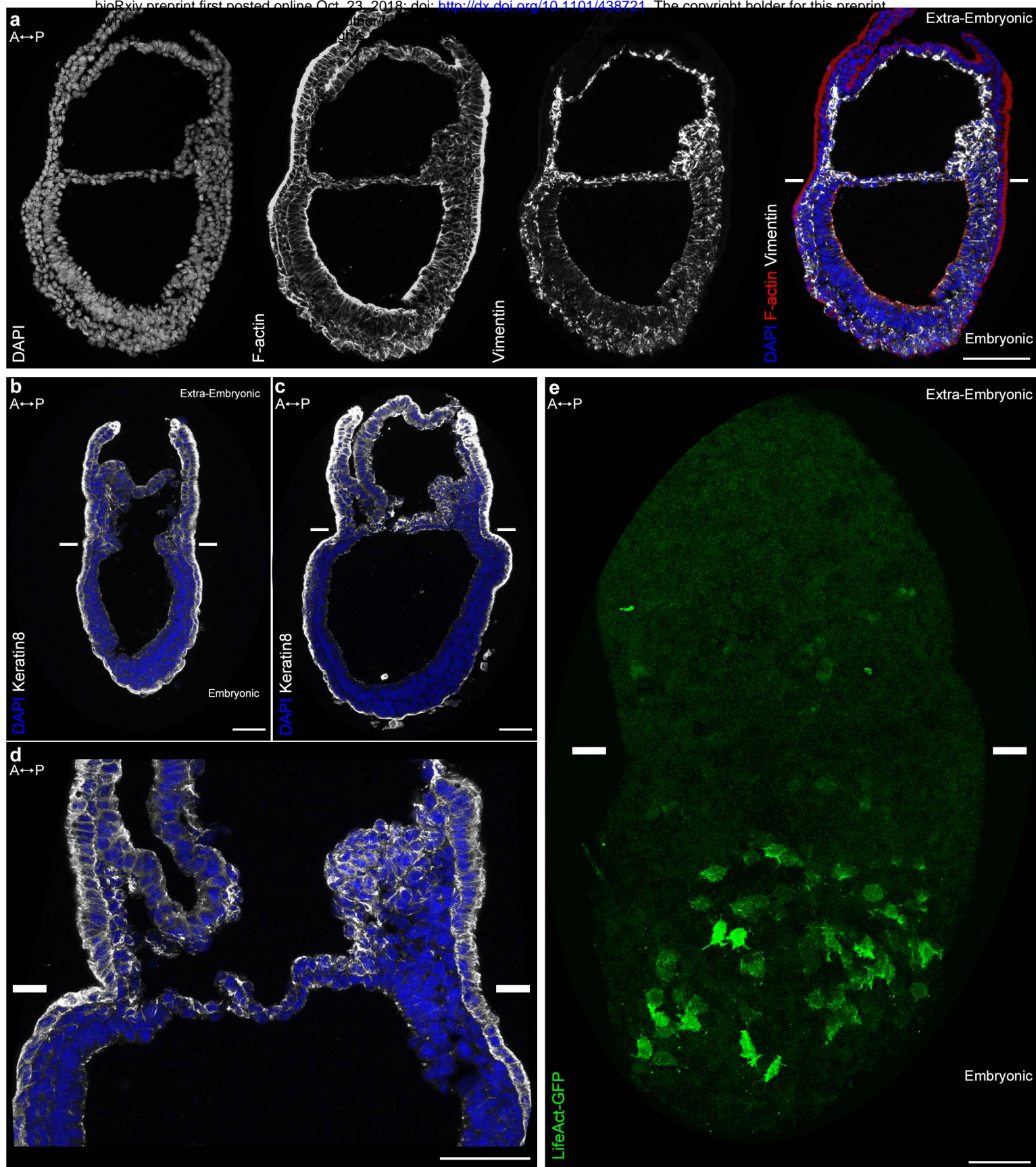


**Figure 5: Embryonic and extra-embryonic mesoderm cells have distinct cytoskeleton composition.** (a) Z-projections of confocal stack of a sagittal section from an Early Bud stage embryo stained for Vimentin, F-Actin (Phalloidin), and nuclei (DAPI). (b, d) Z-projections of confocal stacks of sagittal sections from Late Streak (b) and Early Bud (c: 20x, d: 40x) stages embryos stained for Keratin 8 and nuclei (DAPI). (e) Z-projection of two-photon stack of a whole-mount *T-Cre; LifeAct-GFP* Late Streak embryo. Anterior is to the left. (Scale bars: 50 μm)

288 are major regulators of cytoskeletal rearrangements (Hall, 1998), and the spatiotemporal  
289 fine regulation of Rho GTPases activities determines cytoskeletal dynamics at the  
290 subcellular level (Spiering & Hodgson, 2011). Therefore, inactivation of a given Rho  
291 GTPase may result in variable consequences depending on cell type and context. We  
292 previously established that Sox2-Cre mediated deletion of *Rac1* in the epiblast before  
293 onset of gastrulation causes impaired migration of embryonic mesoderm while extra-  
294 embryonic mesoderm migration is less severely affected (Migeotte et al., 2011). We thus  
295 hypothesized that Rho GTPases might be differentially regulated in cells invading both  
296 regions, resulting in some of the observed distinctions in cytoskeletal dynamics, cell  
297 shape and displacement mode.

298  
299 Mutations were induced in cells transiting the primitive streak by crossing heterozygous  
300 wild-type/null *RhoA* (Jackson et al., 2011) or *Rac1* (Walmsley, 2003) animals bearing  
301 the *T-Cre* transgene with animals homozygous for their respective conditional alleles  
302 bearing the mTmG reporter (mutant embryos are referred to as *RhoA* $\Delta$ *mesoderm* and  
303 *Rac1* $\Delta$ *mesoderm*). The phenotypes of *RhoA* $\Delta$ *mesoderm* and *Rac1* $\Delta$ *mesoderm* embryos  
304 were less severe than that of *RhoA* <sup>$\Delta$ *epi*</sup> and *Rac1* <sup>$\Delta$ *epi*</sup> embryos (our unpublished data and  
305 (Migeotte et al., 2011) ) (Sup. Fig. 3). Mutants were morphologically indistinguishable at  
306 E7.5. At E8.5, *RhoA* $\Delta$ *mesoderm* embryos were identified, though with incomplete  
307 penetrance, as being slightly smaller than their wild-type littermates (11/12 mutants had  
308 a subtle phenotype, including 5 with reduced numbers of somites, and 6 with abnormal  
309 heart morphology) (Sup. Fig. 3a). By E9.5, all *RhoA* $\Delta$ *mesoderm* embryos had an  
310 obvious phenotype (12/12 mutants had a small heart, 9/12 had a reduced number of  
311 somites, 2/12 had an open neural tube, 2/12 had a non-fused allantois) (Sup. Fig. 3b).  
312 *Rac1* $\Delta$ *mesoderm* embryos also had subtle phenotypes at E8.5 (15/16 embryos were  
313 slightly smaller than wild-type littermates, 4/16 had a small heart) (Sup. Fig. 3d). *In situ*  
314 hybridization for *Brachyury* showed weaker staining in the tail region in 5/10 mutant  
315 embryos, indicative of reduced presomitic mesoderm (Sup. Fig. 3c). By E9.5, all mutants  
316 had abnormal heart morphology and reduced body length, and 3 embryos out of 9 were  
317 severely delayed (Sup. Fig. 3e). At E10.5, penetrance was complete; 7/7 embryos had a

318 short dysmorphic body and pericardial edema (not shown). The phenotypic variability at  
319 early time points likely reflects mosaicism of *T-Cre* mediated recombination.

320  
321 Embryonic mesoderm explants from E7.5 MS/LS mTmG; *Rac1* $\Delta$ mesoderm or  
322 *RhoA* $\Delta$ mesoderm embryos were plated on fibronectin. In wild-type explants, cells  
323 showed a radial outgrowth of the explants, displaying large lamellipodia in the direction  
324 of migration (Video 9). After cell-cell contact, they remained connected through long thin  
325 filaments. *RhoA* deficient explants showed no outgrowth of individual cells (Sup. Fig.  
326 4a). *RhoA* mutant cells appeared more cohesive and displayed fewer protrusions than  
327 wild-type cells. Remarkably, live imaging of *RhoA* deleted explants showed a phase of  
328 compaction preceding cell migration (Video 10; 2/4 *RhoA* $\Delta$ mesoderm mutant explants  
329 displayed compaction). In *Rac1* explants (Sup. Fig. 4b), GFP-expressing cells remained  
330 within the domain of the dissected explant and displayed pycnotic nuclei, while wild-type  
331 non-GFP cells could migrate. Live imaging could not be performed as 4 out of 5 mutant  
332 explants detached from the plate. This is similar to explants from *Rac1* epiblast-specific  
333 mutants (Migeotte et al., 2011), and is attributed to lack of adhesion-dependent survival  
334 signals.

335  
336 Live imaging of mTmG; *RhoA* $\Delta$ mesoderm or *Rac1* $\Delta$ mesoderm embryos dissected at  
337 E6.75 or 7.25 (Fig. 6) showed that the majority of *RhoA* and *Rac1* mesoderm-specific  
338 mutants (4/8 for *RhoA*, 6/9 for *Rac1*) displayed an accumulation of cells at the primitive  
339 streak, which formed a clump on the posterior side between epiblast and visceral  
340 endoderm (Fig. 6a, b and Video 11), indicating a mesoderm migration defect.  
341 Interestingly, although embryonic mesoderm migration was impaired, with only a handful  
342 of cells visible on the anterior side by E7.5, extra-embryonic mesoderm migration was  
343 maintained (Fig. 6a', b' and Videos 12, 13). Accordingly, staining for mesoderm-derived  
344 vascular structures (Pecam-1) in the yolk sac at E8.5 showed no difference between  
345 mutants and wild-type embryos (Sup. Fig. 4c, d). Those findings suggest that extra-  
346 embryonic mesoderm cells do not rely on *Rac1* and *RhoA* for movement, which is  
347 consistent with their paucity in actin-rich protrusions.

348

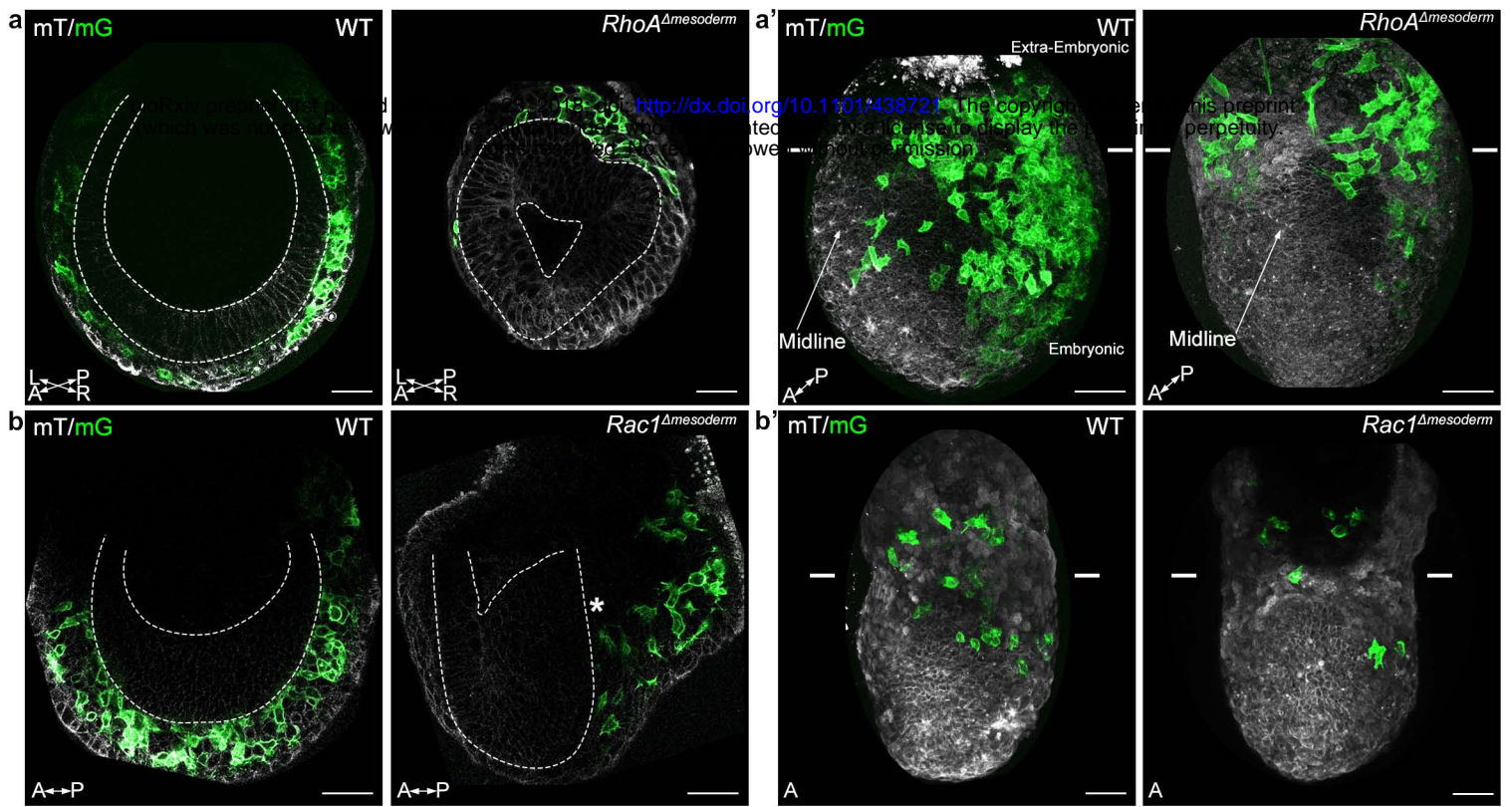


**Figure 6: *RhoA* and *Rac1* mesoderm-specific mutants display impaired migration of embryonic mesoderm.** (a) Frontal optical slice of a *RhoA* $\Delta$ mesoderm embryo and (b) sagittal optical slice of a *Rac1* $\Delta$ mesoderm embryo highlight accumulation of mesoderm cells next to the primitive streak (\*). Dashed lines mark the epiblast. (a' and b') Z-projections of stacks from (a') a *RhoA* $\Delta$ mesoderm embryo (oblique anterior view, posterior to the right, two-photon) and (b') a *Rac1* $\Delta$ mesoderm embryo (anterior view, confocal) show impaired mesoderm migration in embryonic but not extra-embryonic regions. Each mutant is compared to a wild-type littermate in similar orientation. White lines mark the embryonic/extra-embryonic boundary. mG: membrane GFP, in green; mT: membrane dtTomato, in grey. (Scale bar: 50  $\mu$ m).

349 **DISCUSSION**

350 Mesoderm cell delamination from the epiblast requires basal membrane disruption,  
351 apical constriction, loss of apicobasal polarity, changes in intercellular adhesion, and  
352 acquisition of motility (M. Angela Nieto, Huang, Jackson, & Thiery, 2016). The  
353 transcriptional network and signaling pathways involved in epithelial-mesenchymal  
354 transition are conserved (Ramkumar & Anderson, 2011). However, pre-gastrulation  
355 embryo geometry varies widely between species, which has important consequences on  
356 interactions between germ layers and mechanical constrains on nascent mesoderm  
357 cells (M. L. Williams & Solnica-Krezel, 2017). Live imaging of mouse embryo has  
358 allowed recording posterior epiblast rearrangements, as well as cell passage through  
359 the primitive streak (Ramkumar et al., 2016; M. Williams et al., 2012). Contrary to the  
360 chick embryo, there is no global epiblast movement towards the primitive streak in the  
361 mouse. However, cell shape changes, including apical constriction and basal rounding,  
362 are similar. Morphological data on mouse mesoderm cells acquired through scanning  
363 electron microscopy of whole mount samples (Migeotte et al., 2011), and transmission  
364 electron microscopy of embryo sections (Spiegelman & Bennett, 1974) revealed an  
365 array of stellate individual cells linked by filopodia containing a lattice of microfilaments.

366  
367 We took advantage of mosaic labeling of nascent mesoderm to define the dynamics of  
368 cell shape changes associated with mesoderm migration. Cells just outside the streak  
369 retracted the long apical protrusion and adopted a round shape with numerous filopodia  
370 making contacts with adjacent, but also more distant mesoderm cells. In mesodermal  
371 wings, cells close to the epiblast were more loosely apposed, and extended fewer  
372 filopodia towards its basal membrane, compared to cells adjacent to the visceral  
373 endoderm, which were tightly packed and displayed numerous filopodia pointing to the  
374 visceral endoderm basal membrane.

375  
376 Cells travelling in a posterior to anterior direction towards the midline displayed long  
377 protrusions, up to twice the cell body size, which extended, retracted, occasionally  
378 bifurcated, several times before the cell body itself initiated movement, suggesting an  
379 explorative behavior. Remarkably, extension of long protrusions was not limited to the

380 first row of cells. Migration was irregular in time and space, as cells often stopped and  
381 tumbled, and displayed meandering trajectories. After division, cells remained attached  
382 by thin protrusions, and followed parallel paths. Contrary to neural crest cells, mesoderm  
383 cells did not show contact inhibition of locomotion.

384  
385 Extra-embryonic mesoderm first accumulates between extra-embryonic ectoderm and  
386 visceral endoderm at the posterior side of the embryo, leading to formation of the  
387 amniochorionic fold that bulges into the proamniotic cavity (Pereira et al., 2011). This  
388 fold expands, and lateral extensions converge at the midline. Accumulation and  
389 coalescence of lacunae between extra-embryonic mesoderm cells of the fold generate a  
390 large cavity closed distally by the amnion, and proximally by the chorion. At LS stage,  
391 extra-embryonic mesoderm forms the allantoic bud, precursor to the umbilical cord, in  
392 continuity with the primitive streak (Inman & Downs, 2007). Extra-embryonic mesoderm  
393 cells had striking differences in morphology and migration mode, compared to  
394 embryonic mesoderm cells. They were larger and more elongated, displayed fewer  
395 filopodia, and almost no large protrusions. They migrated at a similar speed, but in a  
396 much more tortuous fashion, resulting in little net displacement.

397  
398 Direction cues could come from cell-matrix contact, homotypic or heterotypic (with  
399 epiblast or visceral endoderm) cell-cell interaction, diffuse gradients of morphogens,  
400 and/or mechanical constraints. Transcriptome data were compatible with roles for  
401 guidance molecules such as Netrin1 and Eph receptors in directing mesoderm  
402 migration. *EphA4* was strongly expressed in the PS and mesoderm, particularly in the  
403 embryonic region. In *Xenopus*, interaction of EphA4 in mesoderm and Efnb3 in  
404 ectoderm allows separating germ layers during gastrulation (Rohani, Parmeggiani,  
405 Winklbauer, & Fagotto, 2014). *Epha1* and its ligands *Efna1* and 3 had partially  
406 overlapping, but essentially reciprocal compartmentalized expression patterns during  
407 gastrulation (Duffy et al., 2006). In addition, we found abundant *Epha1* expression in  
408 somites and presomitic mesoderm at E8.5 (not shown). Interestingly, *Epha1* KO mice  
409 present a kinked tail (Duffy et al., 2008). The specific and dynamic expression patterns  
410 of *Epha4*, *Epha1*, and their respective ligands during gastrulation are compatible with

411 roles in germ layers separation, including nascent mesoderm specification and  
412 migration. Identification of those potential guidance cues will help design strategies to  
413 better understand how mesoderm subpopulations reach their respective destinations.

414  
415 Visualization and modification of Rho GTPases activity through FRET sensors and  
416 photoactivable variants has shed light on their fundamental role during cell migration in  
417 *in vivo* contexts, such as migration of fish primordial germ cells (Kardash et al., 2010) or  
418 *Drosophila* border cells (Wang, He, Wu, Hahn, & Montell, 2010). Study of a epiblast-  
419 specific mutant showed that Rac1 acts upstream of the WAVE complex to promote  
420 branching of actin filaments, lamellipodia formation, and migration of nascent mesoderm  
421 (Migeotte et al., 2011). Remarkably, extra-embryonic mesoderm cells did not display  
422 leading edge protrusions, and *Rac1* and *RhoA* mesoderm-specific mutants were  
423 deficient for embryonic, but not extra-embryonic mesoderm migration. In addition, F-  
424 actin filaments were more abundant in embryonic mesoderm, reinforcing the hypothesis  
425 that they might rely on distinct cytoskeletal rearrangements.

426  
427 Intermediate filaments are major effectors of cell stiffness, cell-matrix and cell-cell  
428 adhesion, as well as individual and collective migration (Pan, Hobbs, & Coulombe,  
429 2013). Members of type I and II keratin families form obligate heterodimers, which  
430 assemble into filaments (Loschke, Seltmann, Bouameur, & Magin, 2015). Type II  
431 Keratins 7 and 8, and type I Keratins 18 and 19 are the first to be expressed during  
432 embryogenesis. Combined Keratins 8/19 and 18/19 deletions cause lethality at E10  
433 attributed to fragility of giant trophoblast cells (Hesse, Franz, Tamai, Taketo, & Magin,  
434 2000). Deletion of the entire type II Keratins cluster results in growth retardation starting  
435 at E8.5 (Vijayaraj et al., 2009). Recently, knockdown of Keratin 8 in frog mesendoderm  
436 highlighted a role for intermediate filaments in coordinating collectively migrating cells.  
437 Keratin-depleted cells were more contractile, displayed misdirected protrusions and  
438 large focal adhesions, and exerted higher traction stress (Sonavane et al., 2017).  
439 Transcripts for *Keratins 8* and *18*, as well as *Vimentin*, were enriched in extra-  
440 embryonic, compared to embryonic mesoderm. While Vimentin was present in all  
441 mesoderm, Keratin 8 was only detectable in extra-embryonic mesoderm. An

442 antagonistic relationship between Vimentin intermediate filaments and Rac1-mediated  
443 lamellipodia formation has been described (Helfand et al., 2011), and a similar  
444 opposition may exist between Rac1 activity and keratin intermediate filaments (Weber,  
445 Bjerke, & DeSimone, 2012). Extra-embryonic mesoderm cells' elongated morphology,  
446 paucity in lamellipodia, and lack of directional migration may thus result from their high  
447 content in intermediate filaments, and low Rho GTPase activity (Fig. 7). The recent  
448 development of a K8-YFP reporter mouse strain for intermediate filaments (Schwarz,  
449 Windoffer, Magin, & Leube, 2015), and the availability of reliable Rho GTPases FRET  
450 sensors (Spiering & Hodgson, 2011), will be instrumental in dissecting their relationship  
451 in mesoderm.

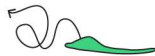
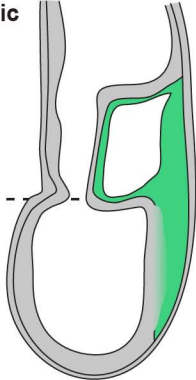
452  
453 The mesoderm germ layer has the particularity to invade both embryonic and extra-  
454 embryonic parts of the conceptus, and its migration is important for both fetal  
455 morphogenesis and development of extra-embryonic tissues including the placenta. We  
456 found that embryonic and extra-embryonic mesoderm populations, both arising by  
457 epithelial-mesenchymal transition at the primitive streak, display distinct shape  
458 dynamics, migration modes, Rho GTPase dependency, cytoskeletal composition, as  
459 well as expression of different sets of guidance, adhesion, and matrix molecules.  
460 Landmark experiments in the 1990s showed that the fate of mesoderm cells depends on  
461 the time and place at which it emerges from the primitive streak. We have unveiled  
462 morphological and behavioral specificities of mesoderm populations through whole  
463 embryo live imaging, and provided a molecular framework to understand how cells with  
464 distinct fates adapt to, and probably modify, their tridimensional environment.

465

## 466 **ACKNOWLEDGMENTS**

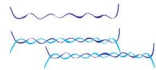
467 We thank the animal house, FACS, and light microscopy (LiMiF) core facilities at the  
468 ULB (Erasme Campus), and the Brussels Interuniversity Genomics High Throughput  
469 core ([www.brightcore.be](http://www.brightcore.be)). We thank M. Martens and J-M. Vanderwinden for confocal  
470 imaging help, A. Lefort and F. Libert for RNA sequencing help, C. Brakebusch, A.  
471 Gossler, V. Tybulewicz, and L. Machesky for kindly sharing mouse lines. B.S. has been  
472 sequentially supported by a fellowship from Erasmus Mundus Phoenix and a fellowship

Extra-Embryonic



Rho GTPases  
independent

Higher abundance of  
intermediate filaments



Embryonic



Rho GTPases  
dependent

Higher abundance of  
F-actin



**Figure 7: Embryonic and extra-embryonic mesoderm cells show distinct forms, trajectories, Rho GTPases dependency, and cytoskeleton composition during gastrulation in the mouse embryo.** In the extra-embryonic region (top), mesoderm cells are stretched, with higher Keratin 8 and Vimentin abundance. Their displacement is convoluted and not dependent on Rho GTPases. In the embryonic region (bottom), mesoderm cells are compact with numerous filopodia, and have higher F-actin abundance. Cells have straighter trajectories and require Rho GTPases. The embryo scheme represents a sagittal section with anterior to the left. Green and grey label mesoderm and other layers, respectively.

473 of the FRS/FRIA. N.M. received a fellowship of the FRS/FRIA, as well as support from  
474 the "Fonds David et Alice van Buuren" and the "Fondation Jaumotte-Demoulin". W. N. is  
475 supported by WELBIO. I.M. is a FNRS research associate and an investigator of  
476 WELBIO. WELBIO, the FNRS, and the Fondation Erasme supported this work. The  
477 authors declare no financial or non-financial competing interests.

478

## 479 **AUTHOR CONTRIBUTIONS**

480 B.S., N.M., W.N. and I.M. designed the experiments and performed data analysis. B.S.,  
481 N.M., W.N. and M-L. R. performed experiments. B.S. and W.N. quantified live imaging  
482 data, and W.N. wrote the python scripts providing statistical analysis. W.N. drew the  
483 schemes. M.D. performed statistical analysis of RNASeq data. I.M. wrote the manuscript  
484 with help from B.S. and W.N.

485

## 486 **METHODS**

### 487 **Mouse strains and genotyping**

488 The *T-Cre* line was obtained from Achim Gossler (Feller et al., 2008), the *Rac1* line from  
489 Victor Tybulewicz (Walmsley, 2003), the *RhoA* line from Cord Brakebusch (Jackson et  
490 al., 2011), the mTmG (Muzumdar et al., 2007) line from Jax Laboratory, and the LifeAct-  
491 GFP line from Laura Machesky (Schachtner et al., 2012). Mice were kept on a CD1  
492 background. Mice colonies were maintained in a certified animal facility in accordance  
493 with European guidelines. Experiments were approved by the local ethics committee  
494 (CEBEA).

495 Mouse genomic DNA was isolated from ear biopsies following overnight digestion at  
496 55°C with 1.5% Proteinase K (Quiagen) diluted in Lysis reagent (DirectPCR, Viagen),  
497 followed by heat inactivation.

498

### 499 **Embryo culture and live imaging**

500 Embryos were dissected in Dulbecco's modified Eagles medium (DMEM) F-12 (Gibco)  
501 supplemented with 10% FBS and 1% Penicillin-Streptomycin and L-glutamine and 15  
502 mM HEPES. They were then cultured in 50% DMEM-F12 with L-glutamine without  
503 phenol red, 50% rat serum (Janvier), at 37°C and 5% CO<sub>2</sub>. Embryos were observed in

504 suspension in individual conical wells (Ibidi) to limit drift, under a Zeiss LSM 780  
505 microscope equipped with C Achroplan 32x/0.85 and LD C Apochromat 40x/1.1  
506 objectives. Stacks were acquired every 20 minutes with 3  $\mu$ M Z intervals for up to 10  
507 hours. Embryos were cultured for an additional 6 to 12 hours after imaging to check for  
508 fitness.

509

### 510 **Antibodies**

511 Antibodies were goat anti-Pecam-1 1:500 (R&D systems); rabbit anti-Podocalyxin 1:200  
512 (EMD Millipore); rat anti-Keratin 8 1:100 (Developmental Studies Hybridoma Bank);  
513 rabbit anti-Vimentin 1:200 (abcam). F-actin was visualized using 1.5 U/ml TRITC-  
514 Phalloidin (Invitrogen), and nuclei using DAPI (Sigma). Secondary antibodies were anti  
515 rabbit Alexa Fluor 488 and 647, anti rat Alexa Fluor 647 (all from Life technologies), and  
516 anti goat Alexa Fluor 647 (Jackson).

517

### 518 **Embryo Analysis**

519 Whole-mount *in situ* hybridization was carried out as described in (Eggenschwiler &  
520 Anderson, 2000). For *in situ* hybridization on sections, embryos were dissected in PBS  
521 and fixed for 30 minutes at 4°C in 4% PFA. They were washed in PBS, embedded  
522 directly in OCT (Tissue-Tek), and cryosectioned at 7-10 microns. Slides were re-fixed for  
523 15 minutes on ice in 4% PFA. RNA probes were obtained from ACDBio, and  
524 hybridization was performed using the RNAscope 2.5 HD Reagent Kit-RED (ACDBio)  
525 according to manufacturer's instructions. Slides were counterstained with 50% Gill's  
526 Hematoxylin.

527

528 For immunofluorescence, embryos were fixed in PBS containing 4% paraformaldehyde  
529 (PFA) for 2 hours at 4°C, cryopreserved in 30% sucrose, embedded in OCT and  
530 cryosectioned at 7-10 microns. Staining was performed in PBS containing 0.5% Triton  
531 X-100 and 1% heat-inactivated horse serum. Sections and whole-mount embryos were  
532 imaged on a Zeiss LSM 780 microscope.

533

### 534 **Explant culture and analysis**

535 Primary explant cultures of nascent mesoderm were generated as described in (Burdal,  
536 Damsky, & Pedersen, 1993). Explants were cultured for 24-48 hours in DMEM F-12  
537 supplemented with 10% FBS and 1% Penicillin-Streptomycin and L-glutamine on  
538 fibronectin (Sigma) coated glass bottom microwell 35mm dishes with 1.5 cover glass  
539 (MatTek). They were fixed for 30 minutes in PBS containing 4% PFA prior to staining.  
540 For live imaging, explants were let to adhere for 4-6 hours, and then imaged every 15  
541 minutes for up to 12 hours.

542

### 543 **Image analysis**

544 Images were processed using Arivis Vision4D v2.12.3 (Arivis, Germany). Embryo  
545 contours were segmented manually on each Z-slice and time point, and then registered  
546 using the drift correction tool of Arivis Vision4D. Embryo rotation was adjusted manually  
547 if necessary. We chose embryos where successful registration could be achieved, so  
548 that the embryo's residual slight movements were much smaller than cell displacement.  
549 Similarly, we found embryo growth to be negligible compared to cell displacement (data  
550 not shown). Cells were then manually segmented on each Z-slice and time point by  
551 highlighting cellular membranes using Wacom's Cintiq 13HD.

552

553 Net displacement, path length, speed and angle between two cells were based on the  
554 centroid coordinates of segmented cells from Arivis, and calculated by a homemade  
555 Python script (Python Software Foundation, <https://www.python.org>). To extract speed  
556 behavior, we interpolated the path length curve and derivated it. The path length over  
557 time was closely linear, so we extracted the mean of the speed values. Surface, volume,  
558 long/short axis ratio of 2D inner ellipse, and straightness were calculated by Arivis. 2D Z  
559 projections of late embryos were used to quantify the filopodia length and density.  
560 Filopodia size and density were measured on Icy (de Chaumont et al., 2012) and  
561 analyzed using a homemade Python script.

562

563 Videos were generated using the StackReg ImageJ plugin (Thevenaz, Ruttimann, &  
564 Unser, 1998).

565

566 All data are presented as Mean  $\pm$  SEM. Depending on whether data had a Gaussian  
567 distribution or not, we used either the Mann-Whitney-Wilcoxon or the *t*-test. A *p* value  
568 <0.05 was considered statistically significant.

569

### 570 **Transcriptome analysis**

571 *T*-Cre; mTmG embryos were collected from different mice, and those at the appropriate  
572 stage were pooled. Embryonic and extra-embryonic portions were separated by  
573 manually cutting the embryo with finely sharpened forceps. The embryos were digested  
574 using 2X Trypsin, and pure GFP+ populations were sorted through flow cytometry  
575 (FACSARIA III, BD), directly in extraction buffer. RNA was extracted using the PicoPure  
576 kit (ThermoFisher Scientific). RNA quality was checked using a Bioanalyzer 2100  
577 (Agilent technologies). Indexed cDNA libraries were obtained using the Ovation Solo  
578 RNA-Seq System (NuGen) following manufacturer recommendation. The multiplexed  
579 libraries (18 pM) were loaded on flow cells and sequences were produced using a HiSeq  
580 PE Cluster Kit v4 and TruSeq SBS Kit v3-HS from a HiSeq 1500 (Illumina). Paired-end  
581 reads were mapped against the mouse reference genome (GRCm38.p4/mm10) using  
582 STAR software to generate read alignments for each sample. Annotations  
583 *Mus\_musculus.GRCm38.87.gtf* were obtained from [ftp.ensembl.org](ftp://ftp.ensembl.org).

584

585 For transcript quantification, all the Reference Sequence (RefSeq) transcript annotations  
586 were retrieved from the UCSC genome browser database (mm10). Transcripts were  
587 quantified using the featureCounts (Liao, Smyth, & Shi, 2014) software tool using the  
588 UCSC RefSeq gene annotations (exons only, gene as meta features). Normalized  
589 expression levels were estimated using the EdgeR rpm function and converted to log<sub>2</sub>  
590 FPKM (fragments per kilobase of exon per million mapped reads) after resetting low  
591 FPKMs to 1 to remove background effect. Differential analysis was performed using the  
592 edgeR method (quasi-likelihood tests) (McCarthy, Chen, & Smyth, 2012). The edgeR  
593 model was constructed using a double pairwise comparison between embryonic  
594 mesoderm versus extra-embryonic mesoderm at two different time points (MS and LS).  
595 First, the count data were fitted to a quasi-likelihood negative binomial generalized log-  
596 linear model using the R glmQLFit method. To identify differentially expressed genes,

597 null hypothesis EM\_E7.0 == EEM\_E7.0 and EM\_E7.25 == EEM\_E7.25 were tested  
598 using the empirical Bayes quasi-likelihood F-tests (glmQLFTest method) applied to the  
599 fitted data. The F-test P-values were then corrected for multi-testing using the  
600 Benjamini-Hochberg p-value adjustment method. Transcripts with a greater than  
601 background level of expression (mean log<sub>2</sub> count per million > 0), an absolute fold  
602 change > 2, and a low false discovery rate (FDR < 0.05) were considered as  
603 differentially expressed.

604  
605 The sample visualization map was produced by applying the t-Distributed Stochastic  
606 Neighbor Embedding (tSNE) dimensionality reduction method (Van Der Maaten &  
607 Hinton, 2008) to log<sub>2</sub> FPKM expression levels (all transcripts). The R tSNE method from  
608 'Rtsne' library was applied without performing the initial PCA reduction and by setting the  
609 perplexity parameter to 2. The heatmap was produced using the R heatmap.2 methods  
610 using the brewer.pal color palette. GO analysis was performed using the DAVID  
611 software (Huang, Sherman, & Lempicki, 2009).

612

## 613 REFERENCES

- 614 Arnold, S. J., & Robertson, E. J. (2009). Making a commitment: cell lineage allocation and axis  
615 patterning in the early mouse embryo. *Nature Reviews Molecular Cell Biology*, 10(2), 91–  
616 103. <https://doi.org/10.1038/nrm2618>
- 617 Bae, Y. K., Trisnadi, N., Kadam, S., & Stathopoulos, A. (2012). The role of FGF signaling in  
618 guiding coordinate movement of cell groups guidance cue and cell adhesion regulator? *Cell*  
619 *Adhesion and Migration*, 6(5), 397–403. <https://doi.org/10.4161/cam.21103>
- 620 Burdsal, C. A., Damsky, C. H., & Pedersen, R. A. (1993). The role of E-cadherin and integrins in  
621 mesoderm differentiation and migration at the mammalian primitive streak. *Development*  
622 *(Cambridge, England)*, 118(3), 829–844.
- 623 Chazaud, C., & Yamanaka, Y. (2016). Lineage specification in the mouse preimplantation  
624 embryo. *Development*, 143(7), 1063–1074. <https://doi.org/10.1242/dev.128314>
- 625 Chuai, M., Hughes, D., & J. Weijer, C. (2012). Collective Epithelial and Mesenchymal Cell  
626 Migration During Gastrulation. *Current Genomics*, 13(4), 267–277.  
627 <https://doi.org/10.2174/138920212800793357>
- 628 de Chaumont, F., Dallongeville, S., Chenouard, N., Herve, N., Pop, S., Provoost, T., ... Olivo-  
629 Marin, J.-C. (2012). Icy: an open bioimage informatics platform for extended reproducible  
630 research. *Nat Meth*, 9(7), 690–696. Retrieved from <http://dx.doi.org/10.1038/nmeth.2075>
- 631 Downs, K. M., & Davies, T. (1993). Staging of gastrulating mouse embryos by morphological  
632 landmarks in the dissecting microscope. *Development (Cambridge, England)*, 118(4),  
633 1255–1266.
- 634 Downs, K. M., McHugh, J., Copp, A. J., & Shtivelman, E. (2002). Multiple developmental roles of  
635 Ahnak are suggested by localization to sites of placentation and neural plate fusion in the

- 636 mouse conceptus. *Gene Expression Patterns*, 2(1–2), 27–34.  
637 [https://doi.org/10.1016/S0925-4773\(02\)00349-0](https://doi.org/10.1016/S0925-4773(02)00349-0)
- 638 Duffy, S. L., Coulthard, M. G., Spanevello, M. D., Herath, N. I., Yeadon, T. M., McCarron, J. K.,  
639 ... Boyd, A. W. (2008). Generation and characterization of EphA1 receptor tyrosine kinase  
640 reporter knockout mice. *Genesis*, 46(10), 553–561. <https://doi.org/10.1002/dvg.20434>  
641 Duffy, S. L., Steiner, K. A., Tam, P. P. L., & Boyd, A. W. (2006). Expression analysis of the  
642 EphA1 receptor tyrosine kinase and its high-affinity ligands Efna1 and Efna3 during early  
643 mouse development. *Gene Expression Patterns*, 6(7), 719–723.  
644 <https://doi.org/10.1016/j.modgep.2005.12.007>
- 645 Dumortier, J. G., Martin, S., Meyer, D., Rosa, F. M., & David, N. B. (2012). Collective  
646 mesendoderm migration relies on an intrinsic directionality signal transmitted through cell  
647 contacts. *Proceedings of the National Academy of Sciences*, 109(42), 16945–16950.  
648 <https://doi.org/10.1073/pnas.1205870109>
- 649 Eggenchwiler, J. T., & Anderson, K. V. (2000). Dorsal and Lateral Fates in the Mouse Neural  
650 Tube Require the Cell-Autonomous Activity of the open brain Gene. *Developmental*  
651 *Biology*, 227(2), 648–660. <https://doi.org/https://doi.org/10.1006/dbio.2000.9918>
- 652 Feller, J., Schneider, A., Schuster-Gossler, K., & Gossler, A. (2008). Noncyclic Notch activity in  
653 the presomitic mesoderm demonstrates uncoupling of somite compartmentalization and  
654 boundary formation. *Genes and Development*, 22(16), 2166–2171.  
655 <https://doi.org/10.1101/gad.480408>
- 656 Hall, A. (1998). Rho GTPases and the Actin Cytoskeleton. *Science*, 279(5350), 509 LP-514.  
657 Retrieved from <http://science.sciencemag.org/content/279/5350/509.abstract>
- 658 Helfand, B. T., Mendez, M. G., Murthy, S. N. P., Shumaker, D. K., Grin, B., Mahammad, S., ...  
659 Goldman, R. D. (2011). Vimentin organization modulates the formation of lamellipodia.  
660 *Molecular Biology of the Cell*, 22(8), 1274–1289. <https://doi.org/10.1091/mbc.E10-08-0699>
- 661 Hesse, M., Franz, T., Tamai, Y., Taketo, M. M., & Magin, T. M. (2000). Targeted deletion of  
662 keratins 18 and 19 leads to trophoblast fragility and early embryonic lethality. *Embo J*,  
663 19(19), 5060–5070. <https://doi.org/10.1093/emboj/19.19.5060>
- 664 Hodge, R. G., & Ridley, A. J. (2016). Regulating Rho GTPases and their regulators. *Nature*  
665 *Reviews Molecular Cell Biology*, 17(8), 496–510. <https://doi.org/10.1038/nrm.2016.67>
- 666 Huang, D. W., Sherman, B. T., & Lempicki, R. A. (2009). Systematic and integrative analysis of  
667 large gene lists using DAVID bioinformatics resources. *Nature Protocols*, 4(1), 44–57.  
668 <https://doi.org/10.1038/nprot.2008.211>
- 669 Ichikawa, T., Nakazato, K., Keller, P. J., Kajiura-Kobayashi, H., Stelzer, E. H. K., Mochizuki, A.,  
670 & Nonaka, S. (2013). Live Imaging of Whole Mouse Embryos during Gastrulation: Migration  
671 Analyses of Epiblast and Mesodermal Cells. *PLoS ONE*, 8(7), 4–12.  
672 <https://doi.org/10.1371/journal.pone.0064506>
- 673 Inman, K. E., & Downs, K. M. (2007). The murine allantois: emerging paradigms in development  
674 of the mammalian umbilical cord and its relation to the fetus. *Genesis*, 45(5), 237–258.  
675 <https://doi.org/10.1002/dvg.20281>
- 676 Jackson, B., Peyrollier, K., Pedersen, E., Basse, A., Karlsson, R., Wang, Z., ... Brakebusch, C.  
677 (2011). RhoA is dispensable for skin development, but crucial for contraction and directed  
678 migration of keratinocytes. *Molecular Biology of the Cell*, 22(5), 593–605.  
679 <https://doi.org/10.1091/mbc.E09-10-0859>
- 680 Kardash, E., Reichman-Fried, M., Matre, J. L., Boldajipour, B., Papisheva, E., Messerschmidt,  
681 E. M., ... Raz, E. (2010). A role for Rho GTPases and cell-cell adhesion in single-cell  
682 motility in vivo. *Nature Cell Biology*, 12(1), 47–53. <https://doi.org/10.1038/ncb2003>
- 683 Kinder, S. J., Tsang, T. E., Quinlan, G. A., Hadjantonakis, A. K., Nagy, A., & Tam, P. P. (1999).  
684 The orderly allocation of mesodermal cells to the extraembryonic structures and the  
685 anteroposterior axis during gastrulation of the mouse embryo. *Development*, 126(21),  
686 4691–4701. <https://doi.org/10.1002/aja.1002030109>

- 687 Kinder, S. J., Tsang, T. E., Wakamiya, M., Sasaki, H., Behringer, R. R., Nagy, a, & Tam, P. P.  
688 (2001). The organizer of the mouse gastrula is composed of a dynamic population of  
689 progenitor cells for the axial mesoderm. *Development (Cambridge, England)*, *128*, 3623–  
690 3634.
- 691 Kingsley, P. D., McGrath, K. E., Maltby, K. M., Koniski, A. D., Ramchandran, R., & Palis, J.  
692 (2001). Subtractive hybridization reveals tissue-specific expression of ahnak during  
693 embryonic development. *Development Growth and Differentiation*, *43*(2), 133–143.  
694 <https://doi.org/10.1046/j.1440-169X.2001.00557.x>
- 695 Lacaud, G., & Kouskoff, V. (2017). Hemangioblast, hemogenic endothelium, and primitive  
696 versus definitive hematopoiesis. *Experimental Hematology*, *49*, 19–24.  
697 <https://doi.org/10.1016/j.exphem.2016.12.009>
- 698 Lawson, K. A., Meneses, J. J., & Pedersen, R. A. (1991). Clonal analysis of epiblast fate during  
699 germ layer formation in the mouse embryo. *Development*, *113*, 891–911. [https://doi.org/VL](https://doi.org/VL-113)  
700 - 113
- 701 Liao, Y., Smyth, G. K., & Shi, W. (2014). featureCounts: an efficient general purpose program for  
702 assigning sequence reads to genomic features. *Bioinformatics*, *30*(7), 923–930. Retrieved  
703 from <http://dx.doi.org/10.1093/bioinformatics/btt656>
- 704 Loschke, F., Seltmann, K., Bouameur, J. E., & Magin, T. M. (2015). Regulation of keratin  
705 network organization. *Current Opinion in Cell Biology*, *32*, 56–64.  
706 <https://doi.org/10.1016/j.ceb.2014.12.006>
- 707 McCarthy, D. J., Chen, Y., & Smyth, G. K. (2012). Differential expression analysis of multifactor  
708 RNA-Seq experiments with respect to biological variation. *Nucleic Acids Research*, *40*(10),  
709 4288–4297. <https://doi.org/10.1093/nar/gks042>
- 710 McDole, K., Guignard, L., Amat, F., Berger, A., Malandain, G., Royer, L. A., ... Keller, P. J.  
711 (2018). In Toto Imaging and Reconstruction of Post-Implantation Mouse Development at  
712 the Single-Cell Level. *Cell*, 1–18. <https://doi.org/10.1016/j.cell.2018.09.031>
- 713 Migeotte, I., Grego-Bessa, J., & Anderson, K. V. (2011). Rac1 mediates morphogenetic  
714 responses to intercellular signals in the gastrulating mouse embryo. *Development*, *138*(14),  
715 3011–3020. <https://doi.org/10.1242/dev.059766>
- 716 Muzumdar, M. D., Tasic, B., Miyamichi, K., Li, L., & Luo, L. (2007). A global double-fluorescent  
717 Cre reporter mouse. *Genesis*, *45*(9), 593–605. <https://doi.org/10.1002/dvg.20335>
- 718 Nieto, M. A., Gilardi-Hebenstreit, P., Charnay, P., & Wilkinson, D. G. (1992). A receptor protein  
719 tyrosine kinase implicated in the segmental patterning of the hindbrain and mesoderm.  
720 *Development*, *116*(4), 1137–1150. Retrieved from  
721 [http://www.ncbi.nlm.nih.gov/entrez/query.fcgi?cmd=Retrieve&db=PubMed&dopt=Citation&list](http://www.ncbi.nlm.nih.gov/entrez/query.fcgi?cmd=Retrieve&db=PubMed&dopt=Citation&list_uids=1295734)  
722 [st\\_uids=1295734](http://www.ncbi.nlm.nih.gov/entrez/query.fcgi?cmd=Retrieve&db=PubMed&dopt=Citation&list_uids=1295734)
- 723 Nieto, M. A., Huang, R. Y. Y. J., Jackson, R. A. A., & Thiery, J. P. P. (2016). Emt: 2016. *Cell*,  
724 *166*(1), 21–45. <https://doi.org/10.1016/j.cell.2016.06.028>
- 725 Pan, X., Hobbs, R. P., & Coulombe, P. A. (2013). The expanding significance of keratin  
726 intermediate filaments in normal and diseased epithelia. *Current Opinion in Cell Biology*,  
727 *25*(1), 47–56. <https://doi.org/10.1016/j.ceb.2012.10.018>
- 728 Pereira, P. N., Dobрева, M. P., Graham, L., Huylebroeck, D., Lawson, K. A., & Zwijsen, A.  
729 (2011). Amnion formation in the mouse embryo: the single amniochorionic fold model. *BMC*  
730 *Developmental Biology*, *11*(1), 48. <https://doi.org/10.1186/1471-213X-11-48>
- 731 Ramkumar, N., & Anderson, K. V. (2011). SnapShot: Mouse primitive streak. *Cell*, *146*(3), 488–  
732 488.e2. <https://doi.org/10.1016/j.cell.2011.07.028>
- 733 Ramkumar, N., Omelchenko, T., Silva-Gagliardi, N. F., McGlade, C. J., Wijnholds, J., &  
734 Anderson, K. V. (2016). Crumbs2 promotes cell ingression during the epithelial-to-  
735 mesenchymal transition at gastrulation. *Nature Cell Biology*, *18*(12).  
736 <https://doi.org/10.1038/ncb3442>
- 737 Rohani, N., Parmeggiani, A., Winklbauer, R., & Fagotto, F. (2014). Variable Combinations of

- 738 Specific Ephrin Ligand/Eph Receptor Pairs Control Embryonic Tissue Separation. *PLoS*  
739 *Biology*, 12(9). <https://doi.org/10.1371/journal.pbio.1001955>
- 740 Roycroft, A., & Mayor, R. (2016). Molecular basis of contact inhibition of locomotion. *Cellular and*  
741 *Molecular Life Sciences*, 73(6), 1119–1130. <https://doi.org/10.1007/s00018-015-2090-0>
- 742 Schachtner, H., Li, A., Stevenson, D., Calaminus, S. D. J., Thomas, S. G., Watson, S. P., ...  
743 Machesky, L. M. (2012). Tissue inducible Lifeact expression allows visualization of actin  
744 dynamics in vivo and ex vivo. *European Journal of Cell Biology*, 91(11–12), 923–929.  
745 <https://doi.org/10.1016/j.ejcb.2012.04.002>
- 746 Schwarz, N., Windoffer, R., Magin, T. M., & Leube, R. E. (2015). Dissection of keratin network  
747 formation, turnover and reorganization in living murine embryos. *Scientific Reports*, 5, 1–8.  
748 <https://doi.org/10.1038/srep09007>
- 749 Scialdone, A., Tanaka, Y., Jawaid, W., Moignard, V., Wilson, N. K., Macaulay, I. C., ... Göttgens,  
750 B. (2016). Resolving Early Mesoderm Diversification through Single Cell Expression  
751 Profiling. *Nature*, 535(7611), 289–293. <https://doi.org/10.1038/nature18633>
- 752 Sonavane, P. R., Wang, C., Dzamba, B., Weber, G. F., Periasamy, A., & DeSimone, D. W.  
753 (2017). Mechanical and signaling roles for keratin intermediate filaments in the assembly  
754 and morphogenesis of mesendoderm tissue at gastrulation. *Development*, dev.155200.  
755 <https://doi.org/10.1242/dev.155200>
- 756 Spiegelman, M., & Bennett, D. (1974). Fine structural study of cell migration in the early  
757 mesoderm of normal and mutant mouse embryos (T-locus: t-9/t-9). *J Embryol Exp Morphol*,  
758 32(3), 723–728. Retrieved from <http://www.ncbi.nlm.nih.gov/pubmed/4463226>
- 759 Spiering, D., & Hodgson, L. (2011). Dynamics of the rho-family small GTPases in actin  
760 regulation and motility. *Cell Adhesion and Migration*, 5(2), 170–180.  
761 <https://doi.org/10.4161/cam.5.2.14403>
- 762 Stott, D., Kispert, A., & Herrmann, B. G. (1993). Rescue of the tail defect of Brachyury mice.  
763 *Genes and Development*, 7(2), 197–203. <https://doi.org/10.1101/gad.7.2.197>
- 764 Sutherland, A. E. (2015). Tissue morphodynamics shaping the early mouse embryo. *Seminars*  
765 *in Cell and Developmental Biology*, 55, 89–98.  
766 <https://doi.org/10.1016/j.semcdb.2016.01.033>
- 767 Thevenaz, P., Ruttimann, U. E., & Unser, M. (1998). A pyramid approach to subpixel registration  
768 based on intensity. *IEEE Transactions on Image Processing*, 7(1), 27–41.  
769 <https://doi.org/10.1109/83.650848>
- 770 Van Der Maaten, L. J. P., & Hinton, G. E. (2008). Visualizing high-dimensional data using t-sne.  
771 *Journal of Machine Learning Research*, 9, 2579–2605. [https://doi.org/10.1007/s10479-011-](https://doi.org/10.1007/s10479-011-0841-3)  
772 0841-3
- 773 Vijayaraj, P., Kröger, C., Reuter, U., Windoffer, R., Leube, R. E., & Magin, T. M. (2009). Keratins  
774 regulate protein biosynthesis through localization of GLUT1 and -3 upstream of AMP kinase  
775 and Raptor. *Journal of Cell Biology*, 187(2), 175–184.  
776 <https://doi.org/10.1083/jcb.200906094>
- 777 Viotti, M., Foley, A. C., & Hadjantonakis, A.-K. (2014). Gutsy moves in mice: cellular and  
778 molecular dynamics of endoderm morphogenesis. *Philosophical Transactions of the Royal*  
779 *Society B: Biological Sciences*, 369(1657), 20130547–20130547.  
780 <https://doi.org/10.1098/rstb.2013.0547>
- 781 Walmsley, M. J. (2003). Critical Roles for Rac1 and Rac2 GTPases in B Cell Development and  
782 Signaling. *Science*, 302(5644), 459–462. <https://doi.org/10.1126/science.1089709>
- 783 Wang, X., He, L., Wu, Y. I., Hahn, K. M., & Montell, D. J. (2010). Light-mediated activation  
784 reveals a key role for Rac in collective guidance of cell movement in vivo. *Nature Cell*  
785 *Biology*, 12(6), 591–597. <https://doi.org/10.1038/ncb2061>
- 786 Watson, E. D. (2005). Development of Structures and Transport Functions in the Mouse  
787 Placenta. *Physiology*, 20(3), 180–193. <https://doi.org/10.1152/physiol.00001.2005>
- 788 Weber, G. F., Bjerke, M. A., & DeSimone, D. W. (2012). A Mechanoresponsive Cadherin-Keratin

- 789 Complex Directs Polarized Protrusive Behavior and Collective Cell Migration.  
790 *Developmental Cell*, 22(1), 104–115. <https://doi.org/10.1016/j.devcel.2011.10.013>
- 791 Wilkinson, D. G., Bhatt, S., & Herrmann, B. G. (1990). Expression pattern of the mouse T gene  
792 and its role in mesoderm formation. *Nature*, 343, 657. Retrieved from  
793 <http://dx.doi.org/10.1038/343657a0>
- 794 Williams, M., Burdsal, C., Periasamy, A., Lewandoski, M., & Sutherland, A. (2012). The mouse  
795 primitive streak forms in situ by initiation of epithelial to mesenchymal transition without  
796 migration of a cell population. *Developmental Dynamics*, 241(2), 270–283.  
797 <https://doi.org/10.1002/dvdy.23711>
- 798 Williams, M. L., & Solnica-Krezel, L. (2017). Regulation of gastrulation movements by emergent  
799 cell and tissue interactions. *Current Opinion in Cell Biology*, 48, 33–39.  
800 <https://doi.org/10.1016/j.ceb.2017.04.006>
- 801 Zhang, H., Nieves, J. L., Fraser, S. T., Isern, J., Douvaras, P., Papatsenko, D., ... Baron, M. H.  
802 (2014). Expression of Podocalyxin separates the hematopoietic and vascular potentials of  
803 mouse ES cell-derived mesoderm. *Stem Cells (Dayton, Ohio)*, 32(1), 191–203.  
804 <https://doi.org/10.1002/stem.1536>
- 805  
806

## 807 LEGENDS FOR VIDEOS

808

809 **Supplementary Video 1: Mesoderm cells migrating towards extra-embryonic and**  
810 **embryonic regions.** Z-projections of confocal stacks from a *T-Cre*; mTmG embryo  
811 dissected at E6.75 (Early Streak stage) and imaged for 320 min. Mesoderm cells  
812 express membrane GFP (green); all other cells express membrane dtTomato (red).  
813 Anterior oblique orientation with posterior to the right (scale bar: 50  $\mu\text{m}$ ).

814

815 **Supplementary Video 2: "Trial and error" trajectories.** Z-projections of confocal  
816 stacks from a *T-Cre*; mTmG embryo dissected at E6.75 (Mid Streak stage) and imaged  
817 for 260 min. Mesoderm cells express membrane GFP (green); all other cells express  
818 membrane dtTomato (red). Anterior oblique orientation with posterior to the right (scale  
819 bar: 50  $\mu\text{m}$ ).

820

821 **Supplementary Videos 3 and 4: Tracking mesoderm migration.** 3D snapshots of  
822 confocal stacks from *T-Cre*; mTmG embryos dissected at E6.75 (Early Streak stage)  
823 and imaged for 180 min and 160 min, with manually highlighted cells tracked throughout  
824 the time lapse. Videos show highlighted cells first, then the original images (membrane  
825 GFP, in green) in a looping fashion for comparison. All other cells express membrane  
826 dtTomato (grey). Lateral orientation with anterior to the left (scale bar: 50  $\mu\text{m}$ ).

827

828 **Supplementary Video 5: Extra-embryonic mesoderm migration is characterized by**  
829 **low net displacement.** Z-projection of confocal stack from a *T-Cre*; mTmG embryo  
830 dissected at E6.75 (Early Streak stage) and imaged for 860 min cropped to show extra-  
831 embryonic mesoderm cells. Mesoderm cells express membrane GFP (green) (scale bar:  
832 10  $\mu\text{m}$ ).

833

834 **Supplementary Video 6: Mesoderm extends filopodia towards epiblast and**  
835 **visceral endoderm.** Two-Photon stack of a *T-Cre*; mTmG embryo at Late Streak stage.

836 The stack progresses from anterior to posterior. Mesoderm cells express membrane  
837 GFP (green); all other cells express membrane dtTomato (grey) (scale bar: 50  $\mu$ m).  
838

839 **Supplementary Video 7: Searching behaviour.** Z-projection of two-photon stack from  
840 a *T-Cre*; mTmG embryo at Mid Streak stage imaged for 100 min. Arrow points at  
841 embryonic mesoderm cell. Mesoderm cells express membrane GFP (green); all other  
842 cells express membrane dtTomato (grey) (scale bar: 50  $\mu$ m).  
843

844 **Supplementary Video 8: LifeAct-GFP expression is higher in embryonic**  
845 **mesoderm.** 3D snapshots of two-photon stacks from a *T-Cre*; LifeAct-GFP embryo  
846 dissected at E7.25 (Late Streak stage) and imaged for 295 min. Images were processed  
847 with the ZEN blue denoise function. LifeAct-GFP (in green) highlights F-actin. The bright  
848 specks in extra-embryonic on the right side are debris. Lateral orientation with anterior to  
849 the left (3D scale bar: 50  $\mu$ m).  
850

851 **Supplementary Video 9 and 10: *RhoA* $\Delta$ mesoderm explants undergo compaction**  
852 **before cell migration compared to wild type.** Z-projection of confocal stack of  
853 mesoderm explants from *T-Cre*; mTmG (9) and *T-Cre*; mTmG; *RhoA* fl/- (10) embryos  
854 dissected at E7.5 (Late Streak stage). Explants were imaged for 750 min every 15 min.  
855

856 **Supplementary Video 11: *RhoA* $\Delta$ mesoderm embryos display an accumulation of**  
857 **mesoderm near the primitive streak.** Two-photon Z stack of a *T-Cre*; mTmG; *RhoA* fl/-  
858 embryo at Late Streak stage. Mesoderm cells express membrane GFP (green); all other  
859 cells express membrane dtTomato (grey). Anterior oblique orientation with anterior to  
860 the left (scale bar: 50  $\mu$ m).  
861

862 **Supplementary Video 12: Mesoderm migration tracking in a *RhoA* $\Delta$ mesoderm**  
863 **embryo.** 3D snapshots of two-photon stacks from a *T-Cre*; mTmG; *RhoA* fl/- embryo  
864 dissected at E7.25 (Mid Streak stage) and imaged using 2-Photon confocal microscopy  
865 for 120 min showing highlighted cells, which are tracked throughout the time lapse. The  
866 video shows the highlighted cells first, then the original images (Membrane GFP, in  
867 green) in a looping fashion for comparison. All other cells express membrane dtTomato  
868 (grey). Anterior oblique orientation with anterior to the left (scale bar: 50  $\mu$ m).  
869

870 **Supplementary Video 13: Mesoderm migration tracking in *Rac1* $\Delta$ mesoderm**  
871 **embryos.** 3D snapshots of two-photon stacks from a *T-Cre*; mTmG; *Rac1* fl/- embryo  
872 dissected at E7.25 (Mid Streak stage) and imaged for 80 min showing highlighted cells,  
873 which are tracked throughout the time lapse. The video shows the highlighted cells first,  
874 then the original images (Membrane GFP, in green) in a looping fashion for comparison.  
875 All other cells express membrane dtTomato (grey). Lateral orientation with anterior to  
876 the left (scale bar: 50  $\mu$ m).  
877

## 878 879 LEGENDS FOR SOURCE DATA

880  
881 **Source Data 1. Embryonic and extra-embryonic mesoderm cells tracking:** List

882 detailing individual cells tracking, volume and surface measurement results.

883  
884 **Source Data 2. Embryonic and extra embryonic mesoderm shape measurements**

885  
886 **Source Data 3. Embryonic and extra embryonic mesoderm cells filopodia:**  
887 Filopodia number/cell and filopodia length measurements.

888  
889 **Source Data 4. Mesoderm cells filopodia extended towards Visceral Endoderm**  
890 **and Epiblast.**

891  
892 **Source Data 5. Quantification of mesoderm cellular division.**

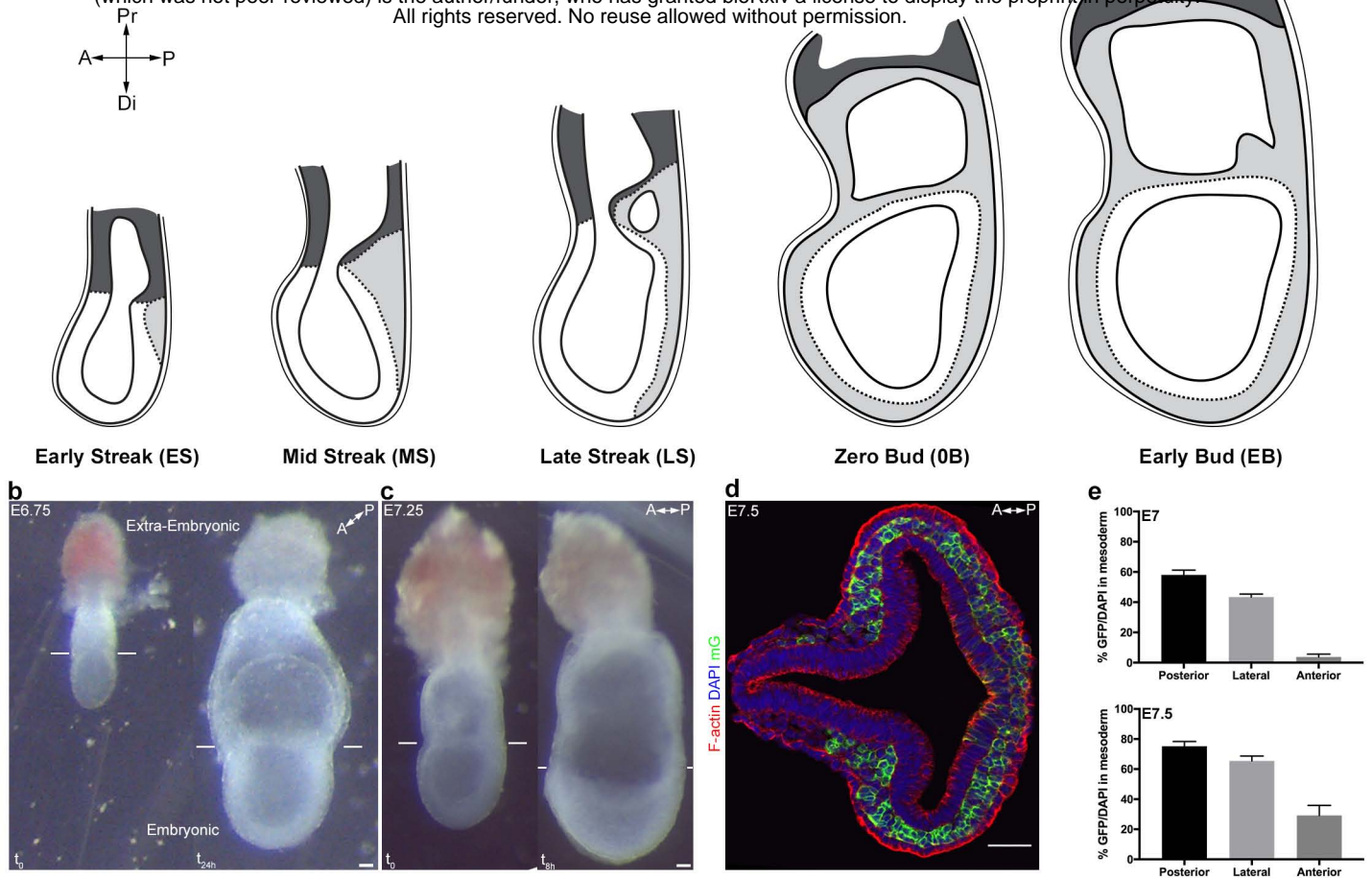
893  
894 **Source Data 6. Quantification of mesoderm cellular collision.**

895  
896 **Source Data 7. Description and quality control of samples used for RNA-seq.** EM:  
897 Embryonic mesoderm; EEM: Extra-Embryonic mesoderm; EC: Embryonic control; EEC:  
898 Extra-Embryonic control.

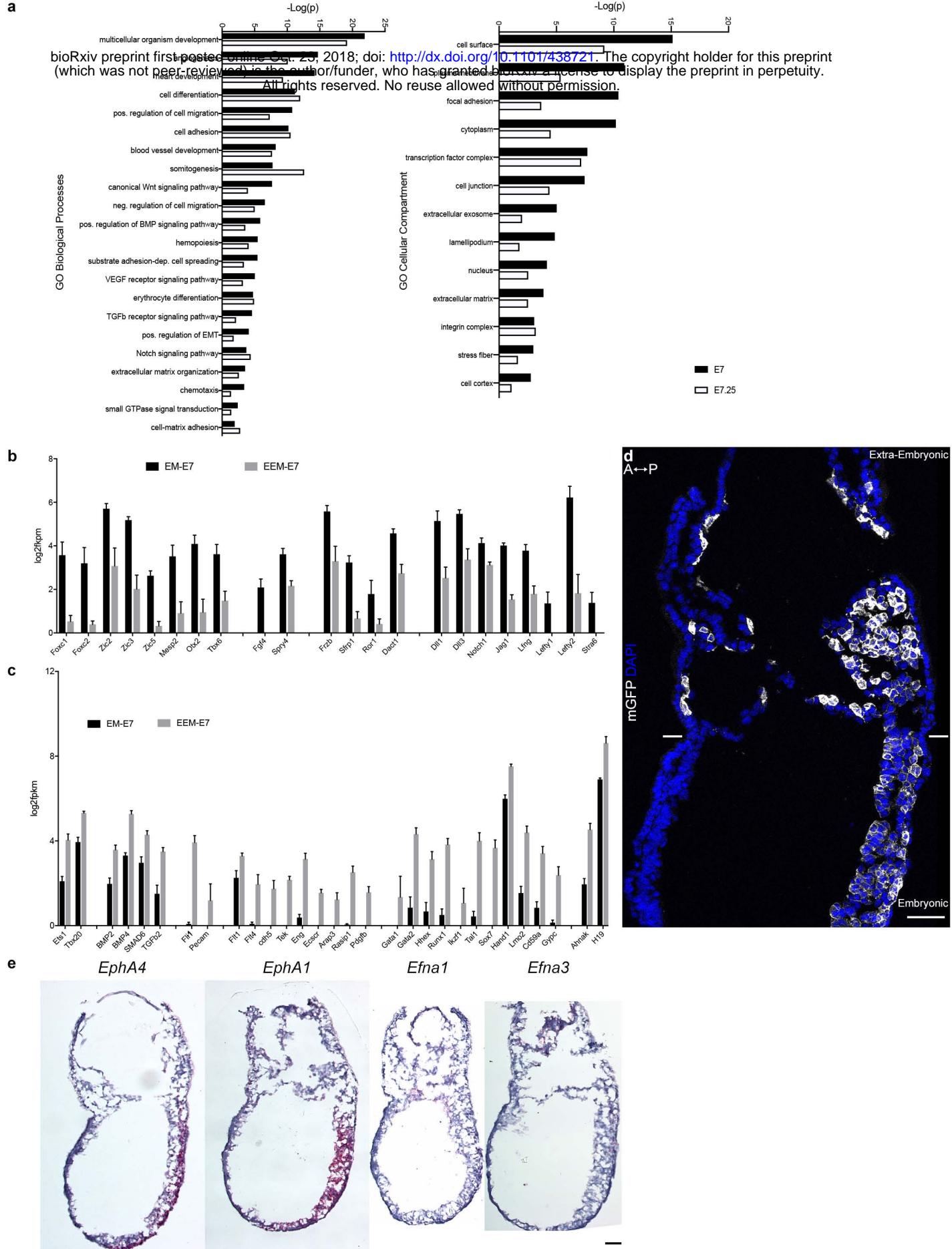
899  
900 **Source Data 8: Expression Levels.** Table containing expression levels in log2 FPKM  
901 computed using the rpkm edgeR method.

902  
903 **Source Data 9: Ranked list of differential expression.** Column 1: gene name,  
904 Column 2 log2 Fold change between EM\_E7.0 and EEM\_E7.0, Column 3 log2 Fold  
905 change between EM\_E7.25 and EEM\_E7.25, Column 4 log2 Count Per Million, Column  
906 5 F-test value, Column 6 F-test pvalue, Column 7 F-test FDR (Benjamini-Hochberg).

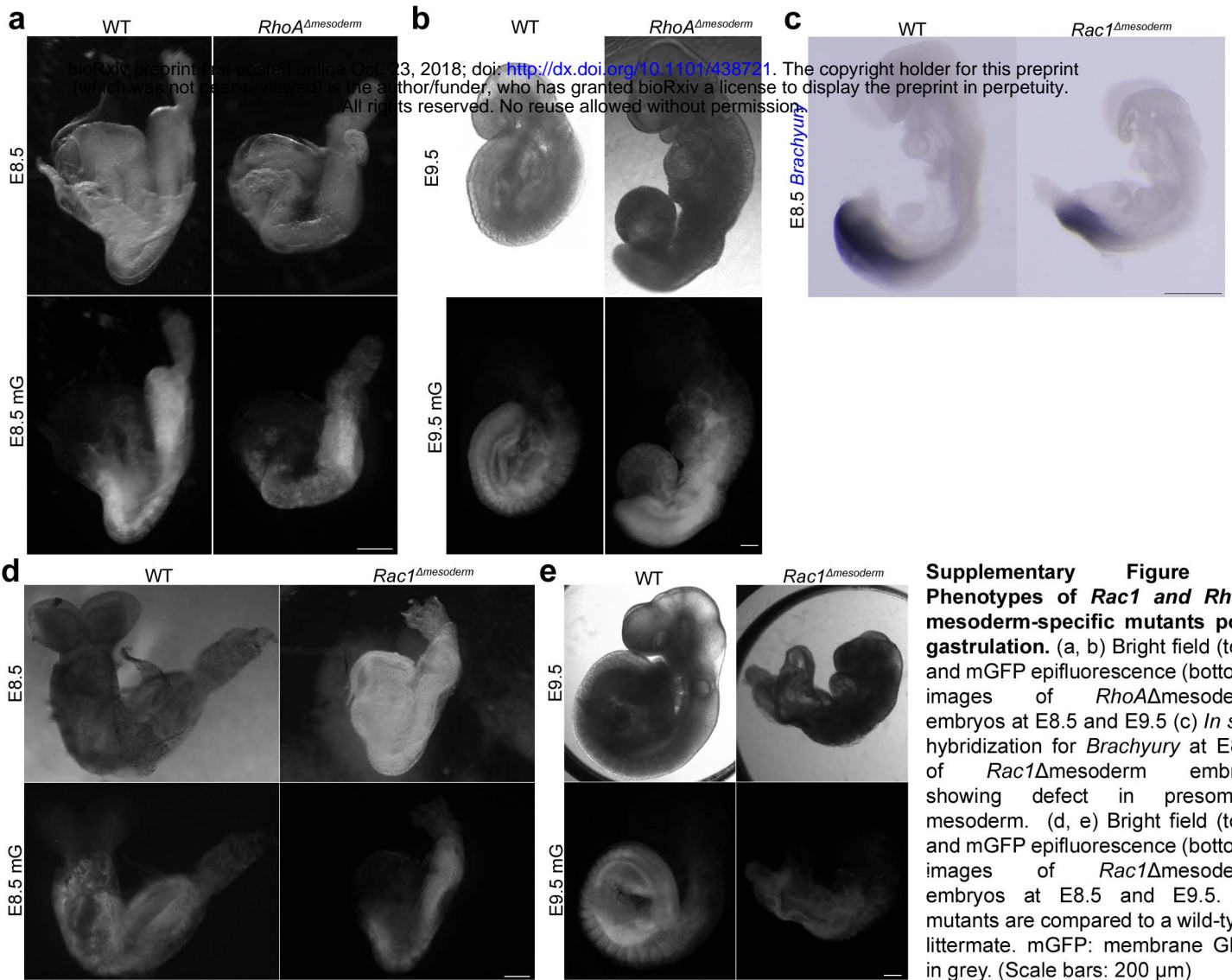
a bioRxiv preprint first posted online Oct. 23, 2018; doi: <http://dx.doi.org/10.1101/438721>. The copyright holder for this preprint (which was not peer-reviewed) is the author/funder, who has granted bioRxiv a license to display the preprint in perpetuity. All rights reserved. No reuse allowed without permission.

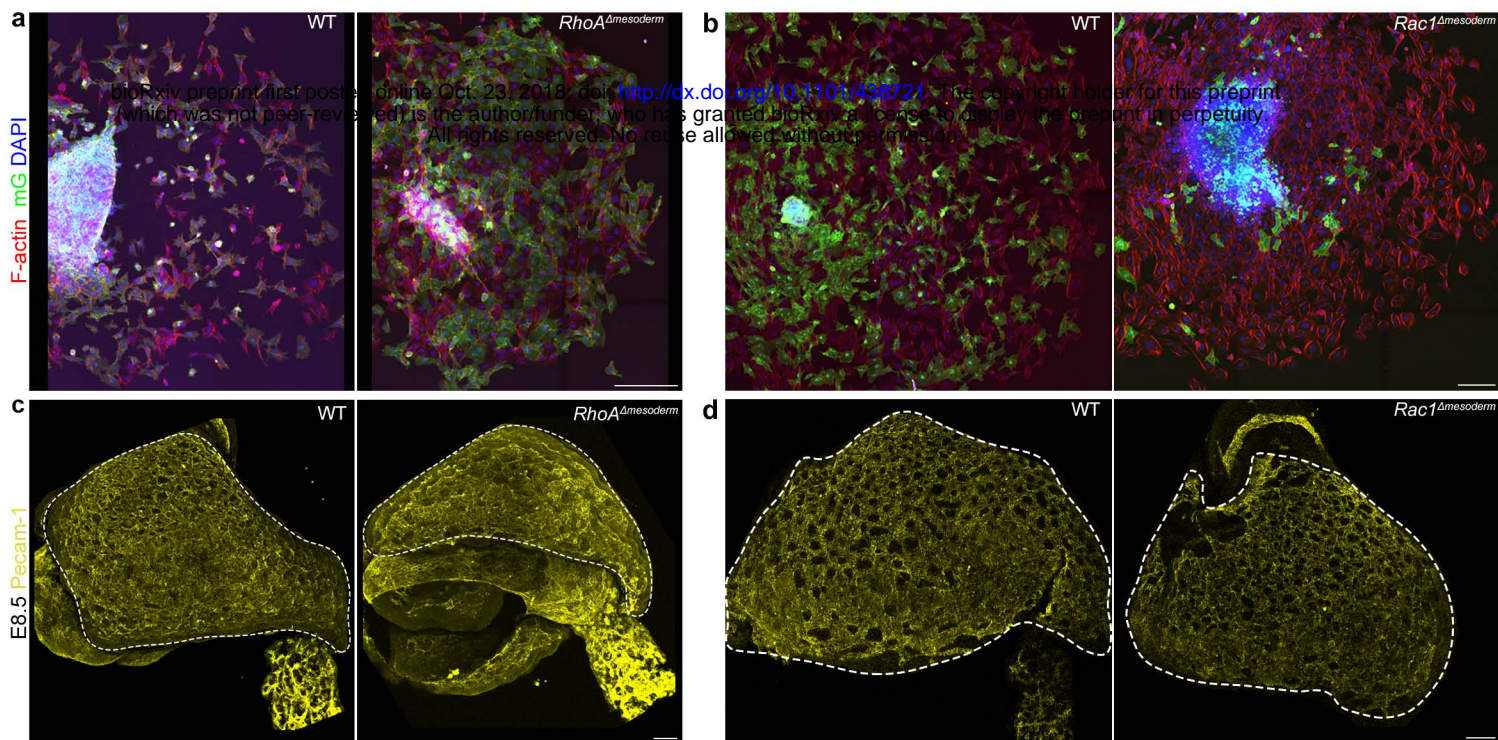


**Supplementary Figure 1: Live imaging of *Brachyury* (*T*)-Cre; mTmG embryos.** (a) Sketches showing mouse embryo anatomical landmarks used for staging between Early Streak and Early Bud stages. (b) *Ex vivo* growth of an embryo dissected at E6.75 (Early Streak stage, left panel), after imaging for 12 hours using confocal imaging plus 12 hours of subsequent culture (Zero Bud stage, right panel). (c) *Ex vivo* growth of an embryo dissected at E7.25 (Late Streak stage, left panel), after 8 hours two-photon imaging (Early Bud stage, right panel). (d) Transverse section at primitive streak level of a E7.5 (Late Streak stage) *T*-Cre; mTmG embryo stained for F-actin (Phalloidin, red) and nuclei (DAPI, blue) (scale bar: 50  $\mu$ m). (e) Quantification of mosaicism as the ratio of GFP+ cells/all cells in the mesoderm layer (identified anatomically between the epiblast and the visceral endoderm) in anterior, posterior and lateral quadrants at different stages of gastrulation: E7 (Mid Streak stage) and E7.5 (Early Bud stage) (mean  $\pm$  SEM, n=5 embryos for each stage). A: Anterior, P: Posterior, Pr: Proximal, Di: Distal, mGFP: membrane GFP, in green.



**Supplementary Figure 2: Embryonic and extra-embryonic mesoderm transcriptome in the mouse embryo.** (a) Gene ontology enrichment of gene clusters related to biological processes and cellular compartments that are differentially expressed between embryonic and extra-embryonic mesoderm with the higher statistical significance at E7 and E7.25. (b,c) Selection of genes known to have higher expression in (b) extra-embryonic or (c) embryonic mesoderm, represented as mean  $\pm$  SEM of log<sub>2</sub> fpkm at E7 (n=4 biological replicates, p<0.001), with embryonic in black and extra-embryonic in grey. EM: Embryonic mesoderm and EEM: Extra-Embryonic mesoderm. Data can be found in Source Data 8 and 9. (d) Optical slice of sagittal section (anterior to the left) from Early Bud stage embryo with membrane GFP in grey and nuclei in blue (DAPI) (Scale bar: 50  $\mu$ m) (e) *In situ* hybridization of sagittal sections (anterior to the left) from Zero to Early Bud stages embryo highlighting transcripts from *EphA4*, *EphA1*, *Efna1* and *Efna3*, represented by red dots (Scale bar: 100  $\mu$ m).





**Supplementary Figure 4: Embryonic and extra-embryonic mesoderm cellular details in *RhoA* and *Rac1* mesoderm-deleted embryos.** (a, b) Embryonic mesoderm explants from (a) mTmG; *RhoA*<sup>Δmesoderm</sup> and (b) mTmG; *Rac1*<sup>Δmesoderm</sup> Mid/Late Streak embryos cultured on fibronectin for (a) 48h and (b) 30h, stained for F-actin (Phalloidin, in red) and nuclei (DAPI, in blue). mG: membrane GFP, in green. (N=3 for *Rac1*, 4 for *RhoA*; similar phenotype in 2/3 mutants for *Rac1* and 3/4 mutants for *RhoA*). (Scale bars: 200 $\mu$ m for a, and 50 $\mu$ m for b). (c, d) Whole-mount E8.5 (c) *RhoA*<sup>Δmesoderm</sup> and (d) *Rac1*<sup>Δmesoderm</sup> embryos stained for Pecam-1 (in yellow). Dashed lines mark the yolk sack. (N=2 for *RhoA*, 8 for *Rac1*). (Scale bars: 100 $\mu$ m). All mutants are compared to a wild-type littermate.